Directing *in-vitro* Paraxial Mesodermal Differentiation of Human iPSCs and Guiding the Alignment of C2C12 Myoblast Differentiation using Photopatterning

General Research Profile

Krithi Vishnu Balaji

MSc. Regenerative medicine and Technology

Utrecht University

1618794

k.v.balaji@students.uu.nl

Daily Supervisor

Ouafa Dahri

Department of Anatomy and Embryology

LUMC Leiden

Principal Investigator

Niels Geijsen

Department of Anatomy and Embryology

LUMC Leiden

Supervisor

Fanny Sage

Department of Anatomy and Embryology

LUMC Leiden

Examiner

Joost Fledderus

Division of Internal Medicine and Dermatology

UMC Utrecht

LUMC Leiden University Medical Center

CONTENTS

ACKNOWLEDGEMENTS

ABSTRACT

Skeletal muscle regeneration is highly impaired in patients suffering from skeletal muscle disorders like muscular dystrophies, volumetric muscle loss or sarcopenia. Clinically relevant *in-vitro* skeletal muscle models are needed to better understand these disorders and develop personalized therapeutic strategies. Closely mimicking the developmental myogenesis and the anisotropic organization of the skeletal muscle tissue are crucial for engineering physiologically accurate *in-vitro* models. In the first part of this study, the paraxial mesoderm differentiation of human induced pluripotent stem cells (hiPSCs) using a non-transgenic protocol was validated. We learned that optimal Matrigel concentrations and starting cell seeding number are crucial for the successful *in-vitro* differentiation of hiPSCs. The second part of the study aimed to achieve aligned differentiation of C2C12 myoblasts confined to line patterns created by photopatterning of ECM proteins. Interestingly, the differentiated myotubes preferentially aligned with a rightward orientation bias deviating from the line patterns. The angle of the rightward orientation bias increased when the spacing between the line patterns was increased. A protocol to binarize immunofluorescence images was developed in this study. Lastly, the orientation of the aligned myotubes were analyzed using two automated tools, Alignment by Fourier Transform (AFT) and OrientationJ. AFT was superior in alignment scoring accuracy and in providing controllable analysis parameters. But OrientationJ outperformed AFT in terms of diversity of quantitative functionalities. The future goal is to develop a 2D platform to train a machine learning algorithm using aligned myotubes confined to pre-defined geometries and orientations that can enable full automation of the orientation analysis process.

Keywords: Muscle Differentiation, iPSCs, C2C12, Photopatterning, Alignment, Image Processing, Orientation Analysis, FFT

LAYMAN'S SUMMARY

In this study, we investigated how to create early skeletal muscle precursor cells from induced pluripotent stem cells (iPSCs) and how to align the muscle fibre formation in a laboratory setting. iPSCs are stem cells that have been generated by reprogramming other cells from a patient to have the ability to become any cell type. Using iPSCs enables researchers to develop personalized treatment models unique to each patient.

Firstly, to create the early skeletal muscle precursor cells, we treated the iPSCs with a cocktail of growth factors and chemicals to direct their differentiation into muscle precursor cells. We used protocols that closely replicate the muscle development in the embryonic stages. We were able to confirm the differentiation of the iPSCs towards the skeletal muscle lineage by validating the expression of relevant genetic markers.

Secondly, we micropatterned parallel lines of cell adhesion proteins on a substrate to help guide the alignment of muscle fibres as they differentiated from the precursor cells. The proper alignment of the muscle fibres is crucial for the healthy functioning of the muscle tissue. The muscle fibres preferentially aligned rightwards deviating from the line patterns. Interestingly, we observed the rightward deviation to increase when we increased the spacing between the line patterns. Lastly, we tested the performance of two automated orientation analysis tools in analyzing the alignment of the muscle fibres.

The future goal of this study is to develop a micropatterned platform that can guide muscle fibre alignment confined to pre-defined shapes and angles. This platform can be used to train a machine-learning software that can fully automate and standardize the orientation analysis process.

Overall, we believe the findings of this study could contribute in a small way to the development of skeletal muscle models in the laboratory that can closely replicate the aligned structure of the native muscle tissue.

LIST OF FIGURES & TABLES

LIST OF ABBREVIATIONS

SM	Skeletal Muscle
hiPSCs	Human Induced Pluripotent Stem Cells
ECM	Extra-cellular Matrix
UV	Ultra Violet
PDMS	Polydimethylsiloxane
LIMAP	Light-induced Molecular Adsorption
DMD	Digital Micromirror Devices
FFT	Fast Fourier Transform
AFT	Alignment by Fourier Transform
RT-qPCR	Quantitative Reverse Transcription Polymerase Chain Reaction
GCDR	Gentle Cell Dissociation Reagent
ITS-X	Insulin Transferrin Selenium Ethanolamine
NEAA	Non-essential Amino Acids
PBS	Phosphate Buffererd Saline
RT	Room Temperature
FBS	Fetal Bovine Serum
HS	Horse Serum
cDNA	Complementary DNA
PLL	Poly-L-Lysine
MQ	Milli-Q
PFA	Paraformaldehyde
GS	Goat Serum

1.1. BACKGROUND

Skeletal muscle (SM) accounts for around half of the total human body mass, thus making it the largest tissue, it is crucial for many mechanical and metabolic functions in the body (1,2). SMs demonstrate an extraordinary regenerative potential facilitated by the underlying satellite cells which get activated as a result of trauma, injury, or disease (3,4). However, this regenerative potential is greatly impaired in patients suffering from volumetric muscle loss, sarcopenia and genetic disorders like muscular dystrophies (5,6). There is a need for personalized therapeutic strategies and physiologically accurate *in-vitro* SM models to better treat and understand SM diseases. A key to closing that gap is by understanding myogenesis during the developmental stages and closely mimicking the process *in-vitro* (2).

1.2. MYOGENESIS

In the developmental phase, SM is said to arise from the somites, formed from segmentation of the paraxial mesoderm (2). The somites then mature into dermomyotome and myotome, within which the fate of the cells is determined, initiating skeletal myogenesis as a result (2,7,8). The myogenic progenitors later get specified as myoblasts, which then differentiate into myocytes (7). These myocytes undergo fusion to form multinucleated myotubes, which then mature forming myofibers (2,7,8). Myogenesis is further subdivided into; i) Primary myogenesis: the formation of neo muscle fibres in the embryonic stage which acts as scaffolding for, ii) Secondary myogenesis: the secondary muscle fibres form in the foetal stage from fusion and maturation of the primary fibres, iii) Adult myogenesis: regeneration and adaptation to cues (9). The various genetic markers expressed at each stage of SM development are summarized in **Figure 1**. Every step of myogenesis is closely regulated by a sensitive interplay of various crucial molecules, growth factors and signalling pathways (2,8). Consequently, reproducing this intricate dance between various signalling molecules and pathways becomes crucial in engineering *in-vitro* SM models that closely mimic the native SM tissue of the human body.

Figure 1: Overview of the sequence of *in-vivo* SM development and the genetic markers corresponding to the progenitors at each stage of differentiation (adapted from (2))

1.2.1. *In-vitro* Myogenesis

Human induced pluripotent stem cells (hiPSCs) are a viable candidate to generate myogenic progenitors *in-vitro*, citing their transcriptional similarities to embryonic stem cells and possibilities to generate patient or disease-specific SM models (9,10).

The *in-vitro* myogenic differentiation of hiPSCs is facilitated broadly by transgenic and non-transgenic approaches. The transgenic approach majorly involves overexpressing specific myogenic factors (PAX3, PAX7 or MyoD) via viral vectors, providing a large population of myogenic progenitors in a relatively short time (9,11). However, this approach does not mimic the *in-vivo* development and poses risks towards therapeutic applications, as it involves genetic modifications (5). Whereas, the non-transgenic approach involves directing myogenic differentiation by stepwise supplementation of growth factors, mimicking the developmental pathway (12,13). The differentiation output of the latter approach is usually lower and protocols take a longer time (8). Yet, optimizing the non-transgenic approach is crucial for generating myogenic progenitors from hiPSCs that are representative of the *in-vivo* system and safer for therapeutic applications (5,12).

1.2.2. Directed Myogenic Differentiation of hiPSCs

Directed differentiation of hiPSCs involves careful sequential supplementation of several small molecules and growth factors to the culture medium to up/down-regulate signalling pathways that are involved in myogenic differentiation (14).

The current directed differentiation protocols of hiPSCs initiate paraxial mesoderm induction by activating Wnt (using GSK3β inhibitor: CHIR-99021) and simultaneously inhibiting BMP (using LDN-193189) to prevent the induced presomitic mesoderm cells from switching to a lateral plate fate (2,9,12,15–17). The treatment results in myogenic progenitors of the dermomyotome and myotome, which when further supplemented with FGF2, HGF and IGF, promotes myoblast proliferation and migration (12,15,16). Lastly, these myoblasts can be terminally differentiated to myotubes by switching them to a serum-deprived media (9,12).

Interestingly, other *in-vitro* protocols have documented myogenic differentiation even in the absence of a BMP inhibitor (18–21). However, the presence of lateral plate markers was not analyzed in these reports (14). The importance of BMP inhibitors in enhancing myogenic differentiation has been emphasized in previous studies, however, a comprehensive comparison between protocols using BMP inhibition and those that do not, is necessary to validate these findings (12,16,22,23).

1.3. C2C12 DIFFERENTIATION

C2C12 is a well-established immortalized cell line of mouse myoblasts commonly used for *in-vitro* SM research (24–27). The popularity of C2C12 among researchers can be attributed to its robustness, ease of handling and quick differentiation in culture. The undifferentiated myoblasts can be easily expanded in a high serum media (10 – 20%) and readily begin to fuse at 80-90% confluency when switched to low-serum conditions (2%), forming mature myotubes in a span of just 4 to 7 days (28,29).

The differentiation of C2C12 myoblasts in serum-deprived conditions is initiated with myogenin expression, during which the cells are still capable of DNA replication and division. Followed by the induction of p21 (cell cycle inhibitor) which leads to cell cycle arrest and the myoblasts terminally differentiate by fusing to form multi-nucleated myotubes (30). Also, the physical characteristics (adherence, stiffness & geometry) of the culture

substrate have been reported to be crucial for the induction of muscle-specific genes during *in-vitro* differentiation of C2C12 myoblasts (31–33).

1.4. ALIGNMENT OF MUSCLE FIBRES

The native SM is a highly structured, hierarchical tissue composed of fascicles, consisting of bundled fibres, made of multi-nucleated myofibrils and myotubes that are organized parallelly in an aligned manner (34). The muscle fibres' highly oriented anisotropic nature contributes considerably to the force-generating capabilities and viscoelastic properties of the SM tissue (35,36). Improper alignment and branching abnormalities in myofibers impair efficient force transduction and are usually a characteristic of a dystrophic or ageing SM tissue (37,38). Thus, it is important to carefully mimic the anisotropic, aligned organization of myofibers to generate physiologically and functionally accurate *in-vitro* SM models (39).

1.4.1. *In-vitro* Alignment

Cells actively interact with the topographical features of their extra cellular matrix (ECM) which greatly influences their morphology and behaviour (40). The aforementioned process by which cells orient and adapt themselves to topological and geometric cues is known as contact guidance (41). In conventional 2D cultures lacking contact guidance, myoblasts tend to grow in unpredictable spiral patterns. When differentiated, this causes inefficient fusion and formation of randomly oriented multibranched myotubes (37,39). A wide range of fabrication techniques, both in 3D and 2D have been explored through the years attempting to direct SM alignment *in-vitro*. **Table 1** summarizes the different fabrication techniques, cell lines and dimensions of the systems that were creatively implemented in various studies to induce aligned differentiation of SM progenitors.

Table 1: Overview of approaches directing *in-vitro* SM alignment

Fabrication technique	Biomaterials	Cell-lines	System dimension	Outcomes	Publication
Spin coating	Cellulose nanowhiskers	C2C12	2D	Radially oriented myotube differentiation directed by the cellulose nanowhiskers' pattern.	(42)
Micropatterning	Fibronectin protein stamp on polystyrene dish	C2C12	2D	Geometric patterning (lines, tori & hybrid) of fibronectin was shown to influence the differentiation of myoblasts, with the hybrid pattern giving the optimum output.	(33)
Micropatterning	Laminin, fibronectin, collagen I/IV stamp on polystyrene dish	C2C12 & hSkMs	2D	Laminin showed better myotube output, with hSkMs uniformly aligning along different line patterns, but C2C12 did the same only on specific line width/spacing.	(43)
Micropatterning	PDMS stencil on polystyrene dish	C2C12	2D	BSA-coated PDMS stencils with a rectangular hole of width 30 – 50 μm were shown optimal for micropatterning	(44)

				single myotubes, which can be recovered by culturing on a thermoresponsive surface.	
Micropatterning	PDMS films	C2C12	2.5D	The wavy PDMS surface of 6 µm in periodicity demonstrated maximum healthy aligned myoblasts and fused myotubes.	(45)
Micropatterning	PDMS & pHEMA films	C2C12	2.5D	PDMS/pHEMA microgrooves shown to promote aligned myotube fusion. 3D proof of concept: aligned myotubes transferred to collagen gel.	(46)
Micropatterning	Thermoresponsive PIPAAm on glass & gelatin	hSkMs	2D to 3D	2D aligned myoblast cell sheets expanded exclusively on the micropatterned thermoresponsive surface were stacked layer-by-layer forming a 3D myotube construct. An anisotropic cell sheet on top is shown to direct the alignment of isotropic cell sheets underneath.	(39)
Electrospinning	Oxygen-hydrocarbon-coated PCL fibres	C2C12	2.5D	Functionalization (hydroxyl/carbonyl/carboxyl) of PCL improved the alignment and differentiation of myotubes.	(47)
Electrospinning & Micropatterning	PEG Hydrogel & Au-NP functionalized PCL fibres	C2C12	2.5D	PCL nanofibers combined with PEG linear micropatterning were shown to influence myotube alignment, with 500 µm micropattern spacing giving the best differentiation result.	(48)
Extrusion 3D printing	Gelatin	C2C12 & hSkMs	2.5D	Simple gelatin substrates with soft extrusion-printed gelatin lines (a couple of hundred µm spacing) are shown to be sufficient to direct the global alignment of myotubes.	(49)
Extrusion 3D printing & acid etching	Fibrin threads	C2C12	2.5D	Fibrin micro-threads with etched microgrooves were suggested to enhance myoblast alignment (Myotube differentiation was not tested).	(40)
Extrusion 3D printing	GelMA & ColMA	C2C12, phM-PCs &	3D	Myotubes embedded in GelMA and ColMA were shown to be aligned in the	(50)

		hASCs		printing direction.	
Extrusion 3D printing	Collagen & Au-NW	C2C12	3D	Au-NW embedded in the bio-ink align in the direction of printing, aided by an electric field. The aligned Au-NW are shown to contact guide myotube alignment.	(51)
Acoustic pat-terning	Collagen & GelMA	C2C12	3D	Ultrasound waves were used to linearly pattern and differ-entiate myoblasts embedded in collagen and GelMA hydro-gels. Aligned bundles of myotubes were generated without material cues.	(52)
Cryo-gelation	Gelatin-carboxymethyl cellulose & carbon-nan-otubes	C2C12	3D	A 3D anisotropic microporous scaffold was shown to form a mature microtissue with func-tional and aligned myotubes.	(53)
Cantilever hy-drogel embed-ding	Fibrin	C2C12	3D	A multi-assay platform of contractile muscle microtis-sues suspended between canti-levers embedded in fibrin hy-drogel is shown.	(54)

Abbreviations: Polydimethylsiloxane (PDMS), Polyhydroxyethylmethacrylate (pHEMA), Poly(N-isopropyl acrylamide) (PIPAAm), Polycaprolactone (PCL), Polyethylene glycol (PEG), Gold nano-particles (Au-NP), Gelatin methacrylate (GelMA), Collagen methacrylate (ColMA), Gold nano-wires (Au-NW), Human skeletal myoblasts (hSkMs), Primary human muscle progenitor cells (phMPCs), Human adipose stem cells (hASCs)

1.4.2. Micropatterning of Biomolecules

The topographical features and biochemical properties of a substrate can greatly influence cell functions *in-vitro* (40). Micropatterning technologies enable the precise deposition of ECM proteins on 2D substrates, allowing improved control over cellular microenvironments (55). The commonly used micropatterning technologies are photolithography and microcontact printing (56,57). The Photolithography (also known as photopatterning) approach (illustrated in **Figure 2A.**) selectively exposes UV light through a mask to project geometric patterns on a substrate coated by a photoresist. The micropatterned substrate is then incubated with ECM proteins and the photoresist is removed before seeding cells (56,58). The microcontact printing approach uses soft elastomers, such as polydimethylsiloxane (PDMS) stamps to transfer micropatterns of ECM proteins on a substrate (illustrated in **Figure 2B.**) (56,58). However, the above approaches are time-consuming and limited in resolution and shapes that can be patterned. The requirement of a photomask and fabrication of PDMS stamps greatly limits the reliability and makes high-throughput applications very tedious.

The above limitations have been addressed by maskless photopatterning technology that uses the light-induced molecular adsorption (LIMAP) method to micropattern proteins (59,60). In the LIMAP approach, a substrate is first treated with an antifouling coating that prevents protein adsorption and is followed by a photo-initiator coating. Upon exposing to UV light,

the photo-initiator can selectively destroy the underlying antifouling layer by photo-scission. The exposed regions can then be selectively treated with proteins for cell adhesion.
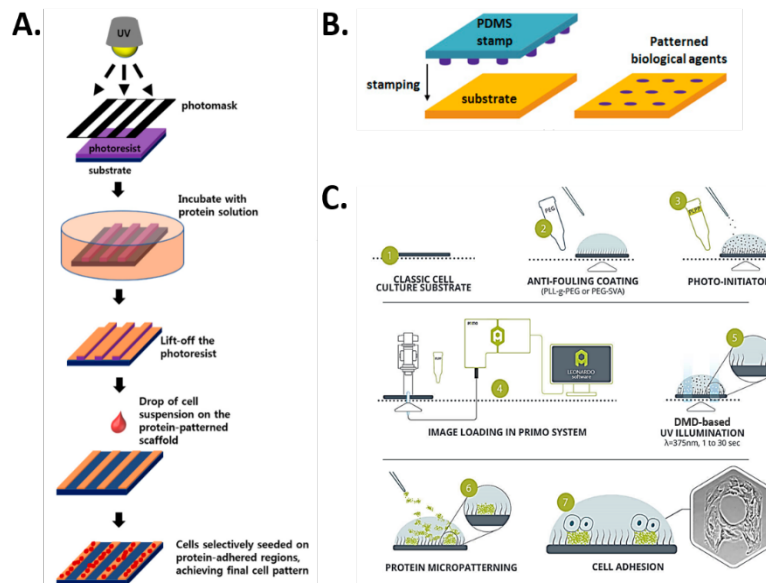
Figure 2: Approaches for micropatterning proteins; (A.) Photolithography using masks (Figure from (58)), (B.) Microcontact printing using PDMS stamps (Figure from (58)), (C.) PRIMO maskless photopatterning using LIMAP (Figure from alveolelab.com).

Moreover, utilizing digital micromirror devices (DMD) for maskless UV projection greatly improves the versatility of the LIMAP approach by enabling the conversion of any grayscale design into a micropattern (59). LIMAP approach by enabling the conversion of any grayscale design into a micropattern (59). PRIMO (Alvéole) is one such system that facilitates high-throughput and high-resolution micropatterning using maskless photopatterning and LIMAP technologies (60). **Figure 2C**. illustrates the micropatterning process using the PRIMO system.

1.4.3. Quantification of Alignment

There has been a necessary transition to 3D *in-vitro* SM models in the field to better recapitulate the native SM environment. However, the transition has shed light on the shortcomings of existing image processing pipelines and tools used to quantify the orientation, fusion index, and distribution of myofibers from microscopic images. Some of the studies on SM alignment employ manual or semi-automated annotation of nuclei and then determine the relative orientation of the nuclear axis to the substrate (40,47,48). Although these methods work, they are time-consuming, prone to error and practically impossible to manually annotate all the cells in a high-density 3D tissue. Some studies have automated the quantification process using MATLAB and other software, but they fail to give a detailed guide (42,46). Some studies do give a detailed elaboration of their processing and quantification algorithm to automate the process but are very difficult to implement for someone who is not proficient with MATLAB or Python (61,62). The 2D Fast Fourier transform (FFT) which converts spatial data into a frequency space to generate orientation distribution, is another popular method, especially for fibrous structures (like myotubes), as it is computationally quick (33,63). However, the conventional 2D FFT only gives a general orientation distribution of an image. It was not designed to recognize cell outlines and also does not give an output of local alignment features within an image (61). There is a need for a standardized image processing guide and openly available software packages that can

automate alignment quantification with minimal user intervention. An ideal tool should be able to accurately assess a wide range of image types, local features within an image and generate a well visualized output of the quantified orientation data.

Acquisition	Preprocessing	Binarization	Alignment Quantification
• Immunofluorescence images: Confocal microscopy	• Adjust contrast and brightness • Filter and despeckle to minimize noise and enhance sharpness	• Perform Global/local thresholding to separate the objects of interest from the background • Convert to 8-bit binary image (black and white signal only)	• Single cell orientation from outline • Orientation from major nuclear axis • Relative orientation distribution: between cells or between cells and environment • Fibre orientation: FFT

Figure 3: General image processing steps for alignment quantification

Different techniques such as relative nuclear orientation, FFT and fibre orientation analysis are used to quantify the alignment of objects in an image. However, to extract the necessary information effectively from microscopic images, it is recommended to carry out some general image processing steps (shown in **Figure 3**) before alignment quantification (61,64).

1.5. RESEARCH OBJECTIVES

The purpose of this study was to investigate *in-vitro* strategies for the development of physiologically accurate SM models. Our study focused primarily on two main objectives:

The first objective was to validate the *in-vitro* differentiation of hiPSCs towards the paraxial mesodermal lineage using a non-transgenic approach. The directed differentiation protocols published by Chal et.al (12) and Cao et.al (65) were tested in this study.

The second major objective was to use photopatterning of ECM proteins to direct aligned differentiation of C2C12 myoblasts. We aimed to establish a 2D platform that would confine myotube alignment to pre-defined shapes and orientations, which could then be used to validate alignment quantification tools. In this study, line patterns of various widths and spacings were created by photopatterning ECM proteins. We hypothesised that the differentiated myotubes would align vertically along the parallel line patterns. An image processing protocol to binarize immunofluorescence images was developed. The performance of two automated orientation analysis tools, Alignment by Fourier Transform (AFT) (66) and OrientationJ (67) in analysing the alignment of myotubes was compared in this study.

2.1. MESODERM DIFFERENTIATION

2.1.1. Differentiation Protocol 1 (Chal et.al)

The directed *in-vitro* SM differentiation protocol published by Chal et.al was closely followed with minor modifications to induce mesoderm differentiation in hiPSCs (12). A double reporter hiPSC line designed by our colleagues was used to assess the differentiation protocol (65). The complete length of the protocol is approximately 40 days to generate terminally differentiated myotubes. However, in this study, we only validate the protocol up until presomitic mesoderm induction, which was one week long.

First, a range of Matrigel coating concentrations was tested to compare their effect on the differentiation outcome. The chosen Matrigel concentration was then used for the next differentiation experiment with a higher cell number. The expression levels of mesodermal markers were evaluated using Quantitative Reverse Transcription PCR (RT-qPCR) from RNA samples collected on different days during the differentiation protocol.

Materials

- **Cell-lines:** hiPSCs - MSGN1-mCherry and PAX3-Venus double reporter line with Blasticidin resistance selection marker (from Orlova group, LUMC)
- **Reagents:** TeSR-E8 (StemCell Technologies, #05990), DMEM/F-12 (ThermoFisher, #11320033), Insulin-Transferrin-Selenium-Ethanolamine (ITS-X) (Gibco, #51500056), MEM Non-Essential Amino Acids Solution (NEAA) (Gibco, 11140050), hESC-Qualified Matrigel Matrix (Corning, #354277), Dulbecco's PBS (ThermoFisher, #14040117), Gentle Cell Dissociation Reagent (GCDR) (StemCell Technologies, #07174), TrypLE Express Enzyme (ThermoFisher, #12605010), TRIzol (Life Technologies, #15596018)
- **Small Molecules:** Blasticidin (Invitrogen, #ant-bl-1), Y27632 (Sigma, #Y0503-5MG), CHIR-99021 (Axon Medchem, #Axon1386), LDN-193189 (Sigma-Aldrich, #SML0559), Human FGF-2 (Peprotech, #100-18B)
- **Equipment:** Falcon 6-well (Corning, #351146), Falcon 12-well (Corning, #353043)

Protocol

Media Formulations
The various media used for the mesoderm induction were formulated as summarised below. The base media were prepared in advance and filtered with a 0.22 µm filter, but the sensitive small molecules (Y-27632, CHIR-99021, LDN-193189, Human FGF-2) were added only on the day of use.

- **E8-b (Maintenance media)**

Components	Volume (50 ml)	Final Concentration
TeSR-E8	49.99 ml	
Blasticidin (10 mg/ml)	10 µl	2 µg/ml

- **E8-bR (Pre-differentiation media)**

Components	Volume (50 ml)	Final Concentration
TeSR-E8	49.9	
Blasticidin (10 mg/ml)	10 µl	2 µg/ml
Y-27632 (5 mM in H_2O)	100 µl	10 µM

- **DIN-CL (Differentiation Media 1)**

Components	Volume (50 ml)	Final Concentration
DMEM/F-12	49	
ITS-X	500 µl	1% (v/v)
NEAA	500 µl	1% (v/v)
CHIR-99021 (10 mM in DMSO)	15 µl	3 µM
LDN-193189 (1 mM in DMSO)	25 µl	0.5 µM

- **DIN-CLF (Differentiation Media 2)**

Components	Volume (50 ml)	Final Concentration
DMEM/F-12	49	
ITS-X	500 µl	1% (v/v)
NEAA	500 µl	1% (v/v)
CHIR-99021 (10 mM in DMSO)	15 µl	3 µM
LDN-193189 (1 mM in DMSO)	25 µl	0.5 µM

hiPSC Maintenance
- 6-well Falcon culture plates were coated for 1 hour at room temperature (RT) with 1:80 (0.14 mg/ml) hESC-qualified Matrigel diluted in cold PBS. (Matrigel aliquots were thawed in ice for 1.5 hours before use)
- A 70% confluent well of hiPSCs (MSGN1-mCherry & PAX3-Venus double reporter line) was aspirated and incubated with 1 ml of GCDR for 4 mins at RT, then aspirated and replaced with E8-b media. The hiPSC colonies were detached carefully using a cell-scraper and collected in a 15 ml tube.
- The colonies were gently resuspended once and plated onto the Matrigel-coated plate at two different concentrations in 2 ml of E8-b media. The media was refreshed daily and the colonies were allowed to expand for at least a week before splitting again.

Mesoderm Differentiation (Testing Matrigel concentrations)
- The 12-well Falcon culture plate was coated for 4 hours on ice with Matrigel concentrations; 0.11 mg/ml, 0.22 mg/ml, 0.44 mg/ml and 0.66 mg/ml, in duplicates respectively. The Matrigel dilutions were prepared in cold DMEM/F-12. The plate was incubated at 37°C for 30 mins and washed with PBS before cell seeding. (Matrigel aliquots were thawed in ice at 4°C overnight before use)
- A 70% confluent well of hiPSC colonies in maintenance was pre-treated for 2 hours with E8-bR media.

- The hiPSC well was washed with PBS, 1 ml of TrypLE Express was added and incubated for 5-7 mins at 37°C, 5% CO_2.
- Once the colonies started dissociating as single cells, they were collected and resuspended gently in a 15 ml tube before adding 10 ml of DMEM/F-12 to deactivate the TrypLE Express. The suspension was spun down at 300g for 5 mins at RT.
- The cell pellet was gently resuspended a couple of times in 1 ml of E8-bR media to form a homogenous suspension of single-cell hiPSCs.
- The cells were counted in Trypan blue using an automated Countess 3 cell counter.
- The cell suspension was diluted in E8-bR media and plated at 9.5 x 10^4 cells in 1.5 ml media per well of the 12-well Matrigel-coated plate.
- The cells were gently redistributed by rocking the plate and incubated at 37°C, 5% CO_2
- The remaining cell suspension was split in 1.5 ml Epis, spun down at 300g for 5 mins and the cell pellets was resuspended in TRIzol (1:3). These TRIzol samples were collected as undifferentiated controls for the hiPSCs. Samples were stored at -20°C.
- The cells were observed and E8-bR media was refreshed daily for 2 days until the hiPSCs reached 15-20% confluent small-sized colonies.
- Day 0: At 15-20% confluency, the cultures were initiated to differentiation by switching to DIN-CL media and refreshed daily until Day 3.
- Day 3: The cultures were switched to DIN-CLF media and refreshed daily until Day 5.
- Day 5: The cultures were dissociated using TrypPLE, spun down at 300g for 5 mins and the cell pellets were resuspended in TRIzol. The TRIzol samples were stored at -20°C.
- The cultures were imaged every other day during the differentiation protocol.

Mesoderm Differentiation (Higher Cell Number)
- The above protocol was repeated with a Matrigel coating concentration of 0.22 mg/ml. 9 wells were coated in total.
- The hiPSCs were plated at an increased number of 1.25 x 10^5 cells per well and undifferentiated control TRIzol samples were collected.
- TRIzol samples were collected on Days 3, 4 and 5 of differentiation, by dissociating 3 wells on each of the days respectively.

The stored TRIzol samples were later processed for RNA isolation and RT-qPCR for tracking the expression levels of mesodermal markers.

2.1.2. Differentiation Protocol 2 (Cao et.al)

The directed *in-vitro* differentiation protocol published by Cao et.al was also explored to induce mesoderm differentiation in hiPSCs (65). This protocol was also one week long. The protocol was tested on two different hiPSC lines seeded at different starting cell numbers.

Materials

- **Cell-lines:** hiPSCs - LUMC30CL12 (from iPS Hotel, LUMC)*,* hiPSCs - LUMC31CL08 (from iPS Hotel, LUMC).
- **Reagents:** mTESR1 (StemCell Technologies, #85850), RevitaCell (RC) Supplement (100x) (Gibco, #A2644501), Matrigel Growth-Factor Reduced (Corning, #354230), XAV-939 (Tocris, #3748-10mg), Iscove's MDM (Life Technologies, #21056), F12 Nutrient Mixture (Life Technologies, #31765), Protein free Hybridoma medium

(PFHMII) (Life Technologies, #12040), Bovine Serum Albumin (BSA) (Bovogen Biologicals, #BSAS 0.1), Lipids (100x) (Life Technologies, #11905031), Monothioglycerol (Sigma-Aldrich, #M6145-25mL), L-Ascorbic acid 2-phosphate (AA2P) (Sigma-Aldrich, #A8960), Glutamax-1 supplement (Life Technologies, #35050)

Protocol

Media Formulation
The mesoderm media (BPEL) was prepared in-house by combining the reagents as shown below and filtered using a 0.22 µm filter and stored at 4°C. The small molecules (CHIR-99021 & XAV-939) were supplemented to the media on the day of use.

- **BPEL Media**

Components	Volume (250 ml)	Final concenctration
IMDM	107.63 ml	
F12 Nut Mix	113.88 ml	
PFHMII	12.5 ml	5%
10% (wt/vol) BSA in IMDM	6.25 ml	0.25%
Lipids (100x)	2.5 ml	1x
ITS-X (100x)	250 µl	0.1x
αMTG solution	750 µl	450 µM
AA2P (5 mg/mL)	2.5 ml	0.05 mg/mL
GlutaMAX (200 mM)	2.5 ml	2 mM
Pen-strep (5,000 U/mL)	1.25 ml	0.5%

hiPSC Maintenance
- The hiPSC (LUMC30CL12 & LUMC31CL08) lines were expanded in 6-well Falcon culture plates coated with 1:80 (0.14 mg/ml) hESC qualified Matrigel, in mTESR1 (1% Pen-Strep) media.
- The colonies were split using GCDR and were allowed to expand for at least a week before splitting again.

Mesoderm Differentiation
- Two 12-well Falcon culture plates were coated for 1 hour at RT with Matrigel (Reduced growth factor) of 83.33 ug/mL (diluted in cold DMEM-F12)   concentration. (Matrigel aliquots were thawed in ice for 1.5 hours)
- A hiPSC maintenance well was washed with PBS, 1 ml of TrypLE Express was added and incubated for 5-7 mins at 37°C, 5% CO_2.
- Once the colonies started dissociating as single cells, they were collected and resuspended gently in a 15 ml tube before adding 4 ml of mTESR1 to deactivate the TrypLE Express. The suspension was spun down at 300g for 5 mins at RT.
- The cell pellet was gently resuspended a couple of times in 1 ml of mTESR1 (1% pen-strep) containing 1:200 RC to form a homogenous suspension of single-cell hiPSCs.
- The cells were counted in Trypan blue using an automated Countess 3 cell counter.

- The cell suspension was diluted in mTESR1 (1% pen-strep) containing 1:200 RC and plated in duplicates of cell numbers: 7.5×10^4, 10×10^4, 12.5×10^4, 15×10^4, 20×10^4, 25×10^4, 30×10^4 per well.
- One Matrigel-coated 12-well plate was seeded with LUMC30CL12 line and the other 12-well plate with LUMC31CL12 line. The cells were allowed to expand for 24 hours.
- Day 0: The cultures were initiated to differentiate by switching them to BPEL containing 8 uM of CHIR-99021.
- Day 1: The cultures were replaced with fresh BPEL containing 8 uM of CHIR-99021.
- Day 2: The cultures were switched to BPEL containing 5 uM of XAV-939.
- Day 3 & 4: The cultures were lastly switched to BPEL containing 4 uM of CHIR-99021.
- The cultures were imaged every 24 hours of the differentiation protocol.

2.2. C2C12 CULTURE AND DIFFERENTIATION

The C2C12 myoblasts were cultured undifferentiated in high serum conditions and upon reaching 90% confluency, the differentiation was initiated by exposing the cells to serum-deprived conditions. The differentiation timeline was traced by evaluating the expression levels of myogenic markers in the samples collected on different days of the protocol. They were also confirmed through immunofluorescence assays.

Materials

- **Cell-lines:** C2C12 murine myoblasts (ATCC)
- **Reagents:** DMEM High glucose (ThermoFisher, #11965092), Fetal Bovine Serum (FBS) (Biowest, #batch-S00F9), Horse Serum (HS) (Gibco, #26050070), 0.25% Trypsin (Gibco, #15050065), ECM Gel (Sigma, #E1270-5ML)
- **Small Molecules:** Penicillin-Streptomycin (Pen-Strep) (10,000 U/mL) (ThermoFisher, #15140122)
- **Equipment:** 10 cm culture dish (Greiner Bio-one, #664160), 12-well culture plate (Greiner Bio-one, #665180)

Protocol

Maintenance

The C2C12 cells were cultured in 10 cm dishes in DMEM with 20% FBS and 1% Pen-Strep (culture media) at 37°C, 5% CO_2. The cells were not allowed to expand beyond 70% confluency and split using Trypsin (0.25%).

Differentiation
- 12-well culture plates were coated with 1:20 ECM gel (diluted in cold DMEM) for 30-40 mins at 37°C, 5% CO_2. The diluted ECM solution was stored at 4°C and reused a maximum of two times within a week. (The ECM gel aliquots were thawed in ice for 1.5 hours before use)
- C2C12 cells from a 70% confluent dish were washed with PBS, trypsinized and plated (50 µl/well from a 2 ml cell suspension) onto the coated 12-well plate and topped up with 1 ml of culture media. The remaining cell suspension was spun down, resuspended in TRIzol and stored at -20°C as undifferentiated control samples.
- Day 0: Once the cultures reached a 90% confluency (after 24-48 hours), the cells were washed with PBS and switched to DMEM with 2% HS and 1% Pen-Strep (differenti-

ation media). The differentiation media was refreshed the following day if a lot of cell death was present.
- The cultures were allowed to differentiate for a length of 8 days and imaged every day.

Experimental Setup
- Four 12-well differentiation experiments were set up on consecutive days, as a representation of four exclusive biological events.
- The cultures were collected using TRIzol from the four plates on specific days (as shown in **Figure 4**) during their respective differentiation cycle. Each Day-point from each of the plates has triplicates (3 wells per Day-point per plate)
- The TRIzol samples were collected in a manner that would result in two biological replicates per Day-point of the differentiation.
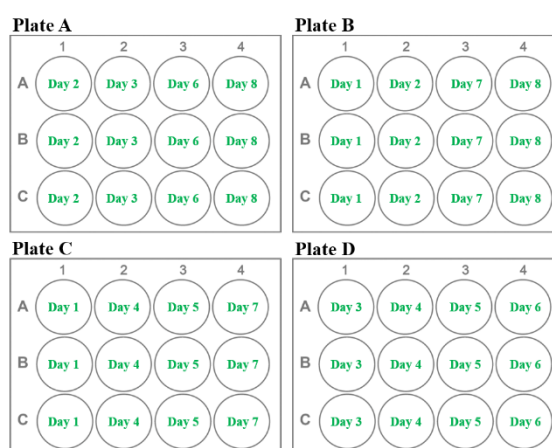
Figure 4: C2C12 Differentiation Experimental Setup; Overview of TRIzol sample collection day-points

- The stored TRIzol samples were later processed for RNA isolation and Real-Time Quantitative Reverse Transcription PCR (RT-qPCR) for tracking the expression levels of myogenic markers.

2.3. RNA ISOLATION

The RNA isolation was performed using the TRIzol-chloroform method and purified using a commercial RNA clean-up concentrator kit. The manufacturer's protocol was closely followed with some modifications.

Materials

Zymo RNA Clean & Concentrator-5 kit (Zymo Research, #R1015), RQ1 RNase-free DNase (Promega, #M6101), Chloroform (Sigma, #C2432), 100% Ethanol (MERK Boom), Tris-HCl (Sigma, #T3253), $MgSO_4$ (Sigma, M7506-500G), $CaCl_2$ (JT Baker, #0064-1KG), UltraPure Agarose (Invitrogen, #16500-500), SYBR-Gold (Invitrogen, #S11494)

Protocol

Sample Preparation
- The stored TRIzol samples were thawed in ice and cold chloroform was added, 0.2 ml per 0.75 ml TRIzol sample.

- The samples were vortexed and incubated for 2 mins before centrifuging at 12000g for 15 mins at 4°C.
- The clear supernatant was carefully transferred to RNase-free Epis and was made ready for RNA clean-up.

Buffer Preparation
- The buffers in the kit used for RNA clean-up were prepared according to the manufacturer's instructions.
- 10X digestion buffer for the RQ1 DNase was prepared according to the manufacturer's instruction; 400 mM Tris-HCl (pH 8), 100 mM $MgSO_4$ and 10mM $CaCl_2$.

Total RNA Clean-up
The samples were processed for RNA clean-up by following the protocol suggested by the manufacturer, with minor modifications in two steps:
- DNase treatment step: 80 µl of the DNase reaction mix (5 µl of DNase in 75 µl of 10X digestion buffer) was added per spin-column.
- RNA elution step: The RNA product was eluted with 50 µl of nuclease-free water.

RNA Product Validation
The concentration and quality of the isolated RNA samples were evaluated using a Qubit 4 fluorometer and agarose gel electrophoresis. The electrophoresis was performed using 200ng of RNA sample in a 1.2% agarose gel (with SYBR-Gold stain) and run at 140V for 30 mins. After validation, the RNA samples were stored at -20°C.

2.4. RT-QPCR ANALYSIS

The expression profiles of the respective differentiation markers were analysed from the RNA samples using RT-qPCR. The complementary DNA (cDNA) was first reverse transcribed from the RNA template. The cDNA was then used as the template for qPCR to record the expression profiles of the differentiation markers using primers specific for the respective genes of interest.

For evaluating the mesodermal differentiation, expression profiles of MSGN1, Tbx6, TbxT and PAX3 genes were quantified. Similarly, expression profiles of Myf5, MyoD, MyoG and Myh1 genes were quantified to evaluate the myogenic differentiation of the C2C12 cells. GAPDH was used as the housekeeping gene for the qPCR reactions and to normalise the expression values of the target genes during analysis.

Materials
SuperScript III First-Strand Synthesis System (Invitrogen, #18080051), iQ SYBR Green Supermix (BioRad, #1708880), Hard-Shell 384-Well PCR Plates (White) (BioRad, #HSP3805), CFX384 Real-Time PCR Detection System (BioRad, #1855484)

Protocol
- The cDNA was reverse transcribed using the SuperScript III system. The manufacturer's protocol was followed to set up the RT-PCR reaction with 400ng of starting RNA template.
- A 1:2 dilution (in nuclease-free water) of the cDNA samples were prepared.
- The qPCR reaction was set up using the Biorad SYBR Green Supermix and CFX384 real-time PCR detection system. The manufacturer's protocol was followed to prepare the qPCR reaction.

- The reactions were set up in a 384 well PCR plate with a 10 µl reaction volume per sample: 5 µl of SYBR Green Supermix, 1 µl of nuclease-free water, 1 µl of forward primer, 1 µl of reverse primer and 2 µl of the cDNA sample.
- The qPCR primer sequences used to quantify the different genes of interest are included in the Appendix (**Table 4A**).
- The obtained C_q values of the differentiated samples were relatively quantified to the C_q values of the undifferentiated control samples using the $\Delta\Delta C_q$ method and normalised against the C_q values of GAPDH.

2.5. PHOTO-MICROPATTERNING

The PRIMO (Alvéole) maskless photopatterning system was used to micropattern ECM proteins in line patterns to possibly direct aligned differentiation of the C2C12 cells. The protocol used in this study was built upon a protocol previously published by the manufacturer for high-throughput micropatterning (68).

Materials

- **Reagents:** Poly-L-lysine (PLL) (Sigma, #P9155-5MG), HEPES (Gibco, #15630080), mPEG-SVA (5kDa) (Laysan Bio, #MPEG-SVA-5000-1g), Triton X-100 (Sigma, #T8787), PLPP Gel (Alvéole), Milli-Q (MQ) water, 70% Ethanol (MERK Boom)
- **Equipment:** µ-Plate 96 square-well black culture plate (ibiTreat) (Ibidi, #89626), µ-Plate 24-well black culture plate (ibiTreat) (Ibidi, #82426), PRIMO System (Alvéole)

Protocol

Pilot Patterning (96 square-well)
- The 96 square-well plate was incubated with 100 µl of PLL solution (250 µg/ml) per well for 1 hour. The wells were then washed thrice with MQ and air-dried.
- A 50 mg/ml mPEG-SVA solution was freshly prepared in 0.1M HEPES buffer (pH 8.2). 100 µl was added to each well and incubated for 1 hour. The wells were washed thrice with MQ and air-dried.
- 2% PLPP gel was prepared in 0.1% Triton X-100 (diluted in MQ) and 80 µl was added to each well. (The PLPP gel was protected from light)
- The plate was put on a hot plate (70 °C) to allow the PLPP gel solution to evaporate and form a transparent layer of gel in each well. (The plate was covered with aluminium foil to protect it from light)
- The PRIMO system was calibrated according to the manufacturer's instructions and the coated plate was mounted on the microscope.
- 6 mm by 6 mm line patterns of various widths and spacings (illustrated in **Figure 5**) were designed on Inkscape and exported as pdf files.
- The designs were imported to the Leonardo software and were photopatterned in duplicates with a 45 mJ/mm^2 UV dose.
- The patterned wells were washed thrice with PBS and incubated with 70% ethanol for 30 mins for sterilization.
- After washing the wells again with PBS, 100 µl of 1:10 ECM gel (diluted in cold DMEM) was incubated for 40 mins at 37°C, 5% CO_2.
- The wells were gently washed with PBS to remove the excess ECM gel and C2C12 were seeded at approximately 2 x 10^3 cells per well in culture media.
- Two of the patterned wells were not seeded and set aside to validate the patterning quality.

- The cells were switched to differentiation media after 24 hours and allowed to differentiate for three days before fixation.
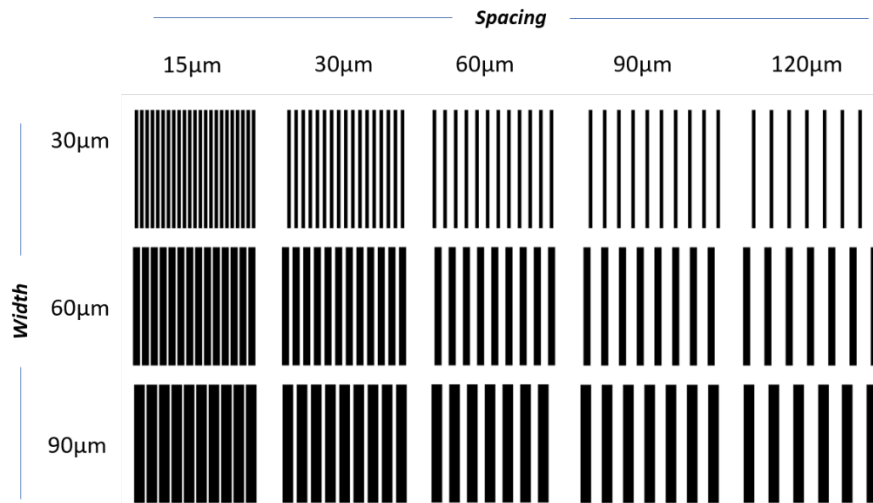
Figure 5: Line patterns of different width and spacing combinations designed for 96 square-well patterning (designs not to scale)

Pilot Patterning (24 circular-well)
- The 24 circular-well plate was prepared following the same protocol as the 96 square-well plate but with increased coating volumes.
- The PLL (250 µg/ml) and mPEG-SVA (50 mg/ml) were added at 160 µl per well.
- The 2% PLPP gel was added at 120 µl per well.
- 8 mm by 8 mm line patterns of various widths and spacings (illustrated in **Figure 6**) were designed on Inkscape and exported as pdf files.
- The designs were photopatterned in duplicates with a 45 mJ/mm^2 UV dose.
- The wells were coated with 200 µl of 1:10 ECM gel, washed with PBS and seeded with C2C12 at approximately 4 x 10^3 cells per well.
- The cells were switched to differentiation media after 24 hours and allowed to differentiate for four days before fixation.
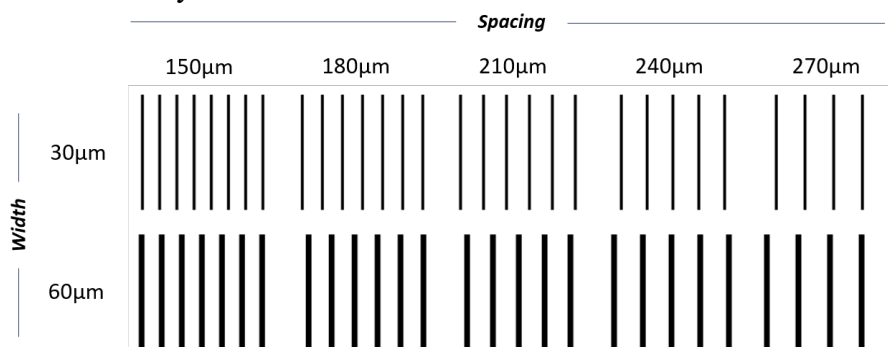
Figure 6: Line patterns of different width and spacing combinations designed for 24 circular-well patterning (designs not to scale)

Optimized Patterning (24-well)
- The 24 circular-well plate patterning was repeated with increased coating volumes.
- The PLL (250 µg/ml) and mPEG-SVA (50 mg/ml) were added at 240 µl per well.
- The 2% PLPP gel was added at 136 µl per well.
- The designs in **Figure 6** were photopatterned with a 45 mJ/mm^2 UV dose.
- The wells were coated with 200 µl of 1:10 ECM gel, washed and seeded with C2C12 at approximately 3 x 10^3 cells per well.

- Three of the patterned wells were not seeded and set aside to validate the patterning quality.
- After 1 hour of seeding, the wells were washed twice with PBS to remove excess cells that were attached to the unpatterned regions.
- The cells were switched to differentiation media after 48 hours and allowed to differentiate for four days.

2.6. IMMUNOFLUORESCENCE ASSAY

Immunofluorescence microscopy was used to validate the differentiation of C2C12 cells by labelling the cells with antibodies specific for the late myogenic markers, myogenin (MyoG) and myosin heavy chain (MHC).

Materials

- **Reagents:** Paraformaldehyde (PFA) (Thermo Scientific, #28908), Goat serum (GS), DAPI, Glycerol (Sigma-Aldrich, #G5516)
- **Primary Antibodies:** Myogenin (M-225) Rabbit polyclonal IgG (Santa-Cruz, #sc-576), Myosin Heavy Chain (MHC) Mouse monoclonal MIgG2b (DSHB, #MF 20-s)
- **Secondary Antibodies:** Donkey anti-Rabbit IgG (H+L) - Alexa Fluor 488 (Invitrogen, #A21206), Donkey anti-Mouse IgG (H+L) - Alexa Fluor 647 (Invitrogen, #A31571)
- **Equipment:** μ-Slide 2 Well (ibiTreat) (Ibidi, #80286), DMi8 Inverted microscope (Leica), Dragonfly 200 Spinning-disc Confocal system (Andor)

Protocol

- The differentiated and undifferentiated (negative control) C2C12 cells were washed with PBS, fixed with 2% PFA for 20-30 mins and washed thrice with PBS (5 mins each time).
- The cells were permeabilized with 0.1% Triton X-100 (diluted in PBS) for 10 minutes on a plate rocker.
- The cells were then blocked with 5% GS (diluted in PBS) for 1 hour on a plate rocker.
- The cells were incubated with 1:200 MyoG and 1:60 MHC primary antibodies (both diluted in 5% GS) overnight at 4°C on a plate rocker.
- Washed thrice with PBS (5 mins each time) the next morning.
- The cells were then incubated in the dark for 1 hour with 1:1000 Alexa 488 anti-Rabbit (for MyoG) and 1:1000 Alexa 647 anti-Mouse (for MHC) secondary antibodies (both diluted in PBS) on a plate-rocker.
- The cells were washed with PBS (5 mins) and incubated in the dark with a nuclear stain, DAPI (1:5000 in PBS) for 5 mins.
- After washing with PBS (5 mins), the immuno-stained cells were mounted in a glycerol medium (1:1 in PBS) and imaged within a week using the Dragonfly 200 confocal microscope system.
- Lasers of the wavelengths 637nm, 488nm and 405nm combined with the Zyla-CF40 camera system were used for the image acquisition.

Unpatterned C2C12 Differentiation: The C2C12 cells were differentiated in unpatterned microscopic slides (2-well Ibidi) and stained for both MyoG and MHC. The images were acquired at 40x magnification, with tile-scan and Z-scan performed when necessary.

Micropatterned C2C12 Differentiation: The C2C12 cells that were differentiated in the line-patterned multi-well plates (96 square-well and 24 well Ibidi) were stained for MHC only. The unseeded wells which were set aside for pattern validation were stained only with the Alexa 647 secondary antibody. The images were acquired at 10x magnification, with tile-scan and Z-scan to cover the patterned regions of each well.

2.7. IMAGE PROCESSING AND ANALYSIS

The acquired immunofluorescence images were pre-processed using the imaging software – Fusion (Andor) and Fiji (ImageJ, NIH). The images of the micropatterning experiments were further processed in Fiji to convert them into binarized images. These images were then used to analyse the myotube fusion index and alignment distribution, which were performed using Fiji plugins and MATLAB tools.

2.7.1. Image Pre-processing

The raw image was first stitched and deconvolved on the Fusion software immediately after acquisition. The '.ims' image file was then opened on Fiji at a level-2 resolution using the Bio-Formats plugin. The Z-slices were projected at maximum intensity to obtain the signal as a 2D image. The brightness and contrast were adjusted separately for both channels (DAPI and MHC) to enhance the signal while minimizing background exposure. Finally, the DAPI and MHC channels of the image were exported as separate '.tiff' files. It was made sure that all the images were cropped to the same size, confining the patterned regions only.

2.7.2. Image Binarization

The binarization protocol implemented using Fiji in this study was developed based on a method previously published by Xu et.al (61). The '.tiff' images (DAPI and MHC channels separately) were first denoised using the despeckle filter and converted to 8-bit format. However, two different thresholding methods had to be implemented for the DAPI and MHC channels respectively to obtain a clear signal. The processing steps used to binarize both channels are summarized in **Table 2** and the Fiji macros of the same are included in the Appendix (**Table 5A**).

Table 2: Binarization processing steps for DAPI and MHC channels

DAPI Channel Binarization	MHC Channel Binarization
1. Process menu: Noise => Despeckle	1. Process menu: Noise => Despeckle
2. Image menu: Type => 8-bit	2. Image menu: Type => 8-bit
3. Image menu: Adjust => Auto-Threshold [Method: *'Default'*, Ignore Black: *'yes'*, White Objects on Black Background: *'yes'*]	3. Image menu: Adjust => Auto-Local Threshold [Method: *'Phansalkar'*, Radius: *'15'*, White Objects on Black Background: *'yes'*]
4. Process menu: Binary => Options [Iterations: *'1'*, Count: *'1'*, Black Background: *'yes'*]	4. Process menu: Binary => Open
5. Process menu: Binary => Make Binary	5. Process menu: Binary => Options [Iterations: *'1'*, Count: *'1'*, Black Background: *'yes'*]
6. File menu: Save as => .tiff (add "DAPI" suffix to the filename)	6. Process menu: Binary => Make Binary
	7. File menu: Save as => .tiff (add "MHC" suffix to the filename)

2.7.3. Myotube Fusion Index

The DAPI and MHC binary '.tiff' images were opened in Fiji and stacked to produce a composite image. The 'analyze particle' function was used to count the particles between 30 -300 size in all three images; DAPI, MHC and DAPI-MHC composite. The image pro-

cessing steps used to perform the analysis are listed in **Table 3** and the Fiji Macro for the same is included in the Appendix (**Table 6A**).

Processing Steps – Particle Analysis
1. DAPI Image - Process menu: Binary => Dilate & Watershed
2. MHC Image - Process menu: Binary => Dilate
3. Image menu: Stacks => Images to Stack [Keep Source Images: *'yes'*]
4. Image menu: Stacks => Z Project [Projection type: *'Max Intensity'*]
5. Analyze menu: Analyze Particles [Size: *'30-300',* Circularity: *'0.00-1.00'*, Show: *'Nothing'*, Summarize: *'yes'*] (*perform for the three open images*)

The Myotube fusion index is determined from the ratio of the number of nuclei present inside the myotubes in relation to the total number of nuclei present in the image. The following formula was used to calculate the myotube fusion index from the particle counts obtained from the three images:

$$Fusion\,Index\,(\%) = \frac{\left(\left(Composite\,count - MHC\,count\right) - DAPI\,count\right)}{DAPI\,count} \times 100$$

The DAPI image particle count gives the total nuclei number, while the composite image particle count gives the nuclei number outside the myotubes. However, some small artefacts from the MHC channel in the composite image are also included in the count. To eliminate the count corresponding to the artefacts, the particle count from the isolated MHC image is subtracted from the composite image count.

2.7.4. Orientation Analysis

The alignment of the differentiated myotubes from the MHC binary image was quantified using two tools that implement the 2D FFT method to obtain orientation information: i) AFT (66), ii) OrientationJ (67).

The AFT is an automated open-source alignment quantification tool that can be easily implemented using MATLAB or Python. The algorithm uses a grid based FFT approach to scan an image in small windows to record local alignment and creates a vector field for the entire image. This vector field is then used to generate an orientation colour map and order parameter. The highlight of this tool is that the user can control the scale over which the features are measured by inputting parameters for the local regions. The performance of the AFT tool was compared to OrientationJ, a Fiji plugin popularly used to quantify alignment. The plugin uses a similar 2D FFT based approach to create a vector field and a colour map for the orientation distribution. The Dominant Direction function of the plugin gives the major orientation direction of the myotubes in the image along with a coherency score.

The AFT tool was implemented on MATLAB (Mathworks, R2022b) following the author's instructions. The MHC binary images were batch processed for analysis using the following parameter settings: Window Size = '*10 px',* Overlap = *'50%'*, Neighbourhood Radius = *'2'*, Save Figures = *'yes'*, Apply Local Filtering & Masking = *'yes',* Masking = *'no'*, Filter Blank Space = *'yes',* Blank Space Threshold = *'0'*, Filter Isotropic Regions = *'no'*.

The OrientationJ plugin was implemented in Fiji to generate the orientation colour map, dominant orientation direction and coherency score using parameters matching the AFT method to generate the vector fields: Local Window σ = *'10 px'*, Gradient = *'Fourier',* Grid Size =

'50'. The dominant orientation direction was used to approximately calculate the angle of deviation of the myotube alignment with respect to the axis of the line patterns.

2.8. STATISTICAL ANALYSIS

Statistical analysis for the qPCR data was performed on Prism (GraphPad, v8). Ordinary one-way ANOVA test was used to analyze the data. Tukey's multiple comparison test was used to compare the significance of differences between the mean of each Day point data with every other Day point data. All the p-values<0.05 were considered significant. With the symbols, '****' for p-values<0.0001, '***' for p-values<0.001, '**' for p-values<0.01, '*' for p-values<0.05 and 'ns' for p-values>0.05. Mean ± Standard deviation values were plotted.

3.1. MESODERM DIFFERENTIATION

3.1.1. Differentiation Protocol 1 (Chal et.al)

The SM differentiation protocol published by Chal et.al was used to direct the mesodermal differentiation of the double reporter (MSGN1-mCherry & PAX3-Venus) hiPSCs. The progress of differentiation of the hiPSCs (seeded at 9.5×10^4 cells) on four different Matrigel concentrations (0.11, 0.22, 0.44 & 0.66 mg/ml) was recorded qualitatively by capturing images on days 0, 2 and 4 of the protocol. In **Figure 7A.** the changes in the morphology of the cultures can be seen; the interconnected hiPSC colonies differentiated into embryoid-like bodies. On day 4, these embryoid-like bodies expressed a red mCherry signal corresponding to MSGN1 expression. On day 0, the colonies appeared to be similar in morphology across the Matrigel concentrations. However, on day 2, the colonies in 0.11 and 0.22 mg/ml Matrigel appeared to be forming embryoid-like bodies. While the colonies in 0.44 and 0.66 mg/ml Matrigel continued to expand as interconnected networks. On day 4, the embryoid-like bodies in 0.11, 0.22 and 0.44 mg/ml were large and similar in size. Whereas, in 0.66 mg/ml Matrigel, there were multiple smaller and dense embryoid-like bodies.
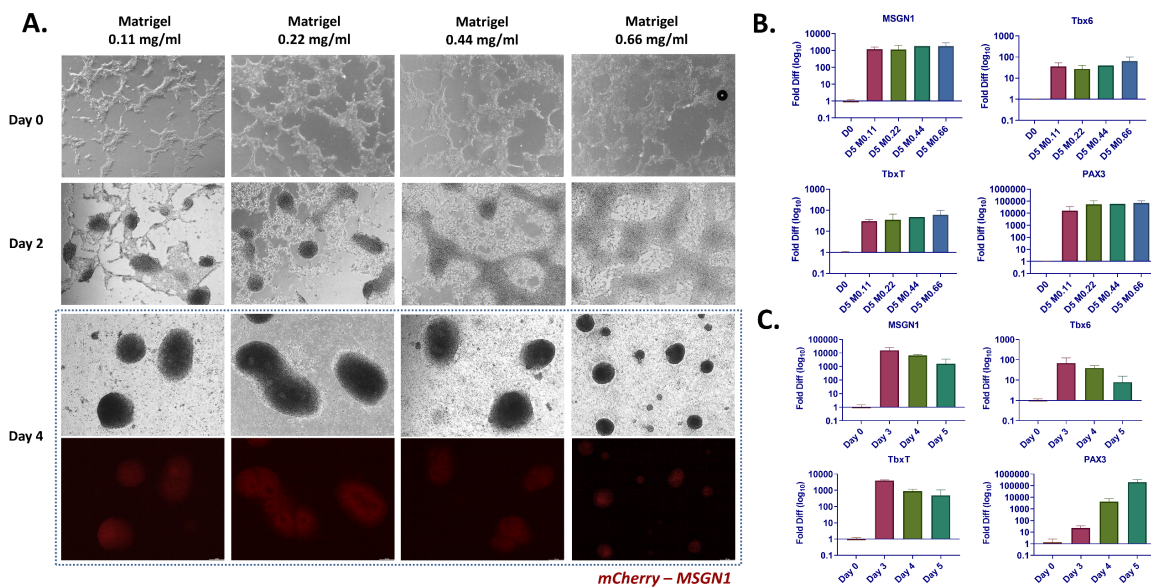
Figure 7: Mesoderm Differentiation Chal. et.al Protocol; (A.) Brightfield images of differentiation progression of the hiPSCs (MSGN1-mCherry & PAX3-Venus reporter line) taken on Days 0, 2 & 4, including red fluorescent channel images for Day 4 (images taken at 4x). (B.) Relative expression levels of MSGN1, Tbx6, TbxT & PAX3 (normalised to GAPDH) on Day 5 of differentiation for 0.11 mg/ml (M0.11), 0.22 mg/ml (M0.22), 0.44 mg/ml (M0.44) & 0.66 mg/ml (M0.66) Matrigel concentrations (fold difference/expression levels were log10 transformed). 1 biological & 6 technical replicates (*3 technical replicates for M0.44) per sample are shown. (C.) Relative expression levels of MSGN1, Tbx6, TbxT & PAX3 (normalised to GAPDH) on Days 0, 3, 4 & 5 of differentiation (fold difference/expression levels were log10 transformed). 1 biological & 6 technical replicates per sample are shown.

The RNA samples isolated from the cultures harvested on different days of the differentiation protocol were subject to RT-qPCR analysis to quantify the mRNA expression levels of the genes responsible for mesoderm induction. MSGN1, Tbx6 and TbxT are mesoderm specification markers and PAX3 can be a marker for dermomyotome, but not exclusively

limited to myogenic determination (9,69). **Figure 7B.** shows the relative expression levels of the above markers between Days 0 and 5 of differentiation of the samples from the different Matrigel concentrations. A very slight upward tick in the expression levels was seen as the Matrigel concentration increased, but it was not significant. **Figure 7C.** demonstrates the relative expression of the markers between Days 0, 3, 4 and 5 of differentiation performed using 1.25×10^5 cells on 0.22 mg/ml Matrigel. The expression levels of MSGN1, Tbx6 and TbxT appeared to go down from Day 3 onwards, while PAX3 expression went up significantly.

3.1.2. Differentiation Protocol 2 (Cao et.al)

The mesoderm differentiation protocol published by Cao et.al was tested on two hiPSC lines (LUMC30CL12 & LUMC31CL08) seeded at different starting cell numbers. The differentiation progress was recorded qualitatively by capturing brightfield images on each day of the protocol. **Figure 8** shows the differentiation progress of the 200K, 250K and 300K starting cell numbers of either hiPSC lines. The differentiation progress of the lower starting cell numbers, 75K, 100K, 125K and 150K is included in the Appendix (**Figure 18A**).
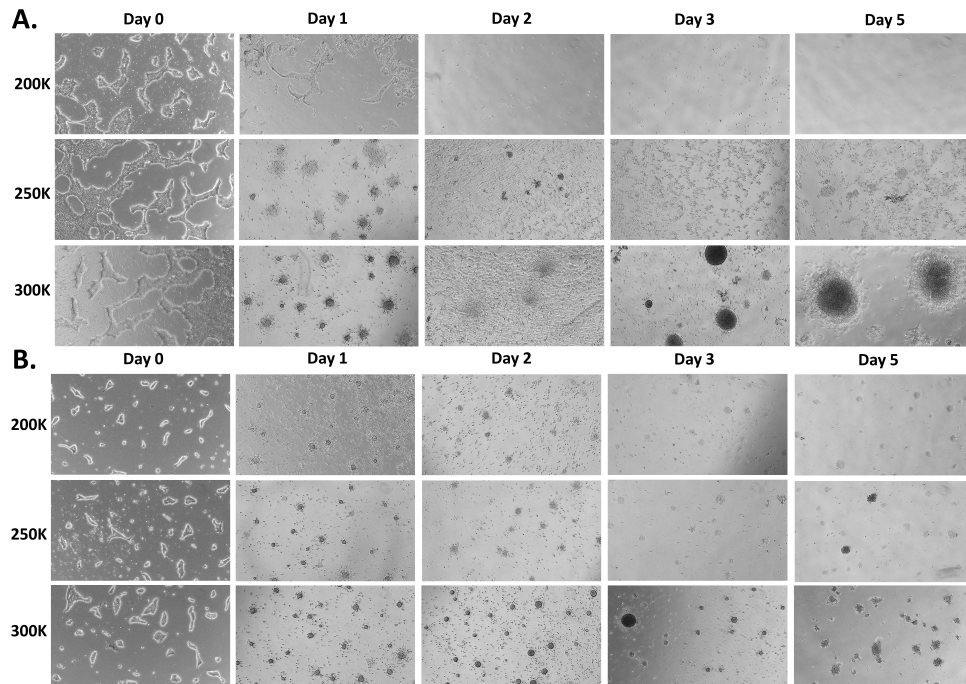
Figure 8: Mesoderm Differentiation Cao. et.al Protocol; Brightfield images of the hiPSCs differentiation progression taken on Days 0, 1, 2, 3 & 5 for the different starting cell numbers of (A.) LUMC30CL12 & (B.) LUMC31CL08 hiPSC lines (images taken at 4x).

Only the 250K and 300K starting cell numbers of either hiPSC lines were observed to remain adherent through the entire length of the differentiation protocol (**Figure 8**). Whereas, the lower starting cell numbers appeared to have fully detached by Day 2 (**Figure 18A**). Notably, the 300K starting cell number of the LUMC30CL12 line (**Figure 8A.**) showed progressive growth of the embryoid-like bodies, while the growth of the LUMC31CL08 line (**Figure 8B.**) plateaued by Day 2. However, it is important to note the differences in the cell colony sizes between the two hiPSC lines on Day 0, even though the starting cell numbers were intended to be the same. The hiPSC colonies on Day 0 of the LUMC31CL08 line (**Figure 8B.**)

appeared to be scarce in comparison to the LUMC30CL12 line (**Figure 8A.**) across the different starting cell numbers.

3.2. C2C12 DIFFERENTIATION

The C2C12 myoblasts were seeded on ECM (1:20) coated plates and allowed to expand in high serum (20% FBS) media. Upon reaching 90% confluency, the cells were switched to serum-deprived (2% HS) media and initiated to differentiate. The progress of differentiation was recorded qualitatively by capturing brightfield images every 24 hours, presented in **Figure 9A.** The myoblasts were seen initiating fusion by Day 2 and formed myotubes between Days 3 to 5 of serum deprivation. Most notably, the myotubes continued to fuse and elongate through Days 6 to 8, with spontaneously contracting myotubes observed by Day 7 of differentiation.
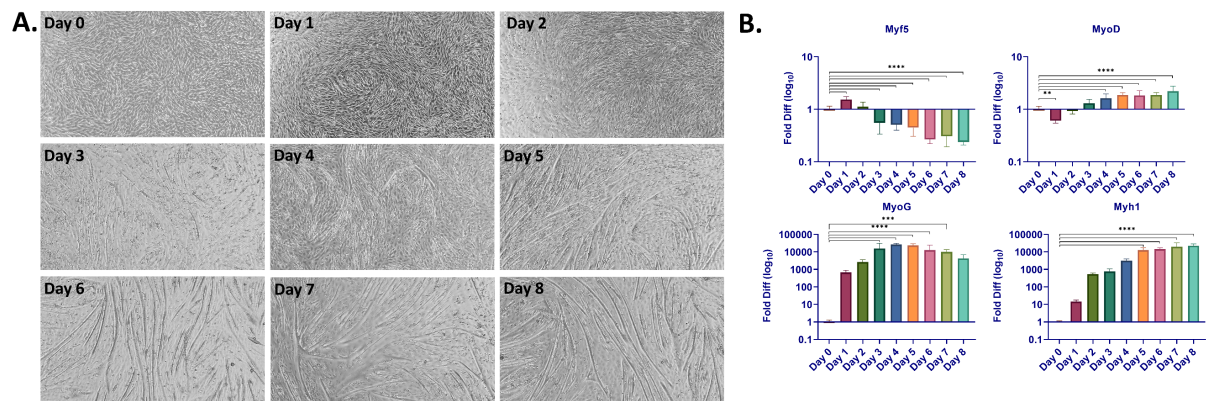
Figure 9: C2C12 Differentiation; (A.) Brightfields images of the differentiating C2C12 myoblasts taken daily from Day 0 to Day 8 (images taken at 4x). (B.) Relative expression levels of Myf5, MyoD, MyoG & Myh1 (normalized to GAPDH) on Days 0, 1, 2, 3, 4, 5, 6, 7 & 8 of differentiation (fold difference/expression levels were log10 transformed). 2 biological & 12 technical replicates (*10 technical replicates for Day 3) per sample are shown.

The RNA samples isolated from the cultures harvested on different days of the differentiation protocol were subject to RT-qPCR analysis to quantify the mRNA expression levels of the genes responsible for myogenic differentiation. Myf5 and MyoD are myoblast determination markers, while MyoG marks the initiation of terminal myogenic differentiation and Myh1 is a late marker of differentiated myotubes (30). **Figure 9B.** illustrates the relative expression levels of the above markers through Days 0 to 8 of differentiation of the C2C12 myoblasts. Myf5 expression was seen to go up slightly on Day 1 and continued to downregulate after. Whereas, MyoD expression was seen to go down slightly on Day 1 and then continued to upregulate a little, plateauing by Day 5. Notably, MyoG expression was highly upregulated on Day 1, peaked by Day 4 and after which it was downregulated. Myh1 expression was observed to be upregulated until Day 6 and plateauing afterwards. Only the results of statistical comparisons between the undifferentiated cells (Day 0) and the differentiated cells (Days 1, 2, 3, 4, 5, 6, 7 and 8) are displayed in the plots in **Figure 9B.** The complete results of the multiple comparison tests between the samples from each day with every other day are summarized in the Appendix (**Tables 7A, 8A, 9A & 10A**).

Immunofluorescence microscopy was used to validate the differentiation of the C2C12 myoblasts by staining for the late myogenic markers MyoG and MHC. **Figure 10A.** illustrates the immunofluorescence images of the C2C12 cells (passage number between 8 to

12) on Day 4 of differentiation. A green signal corresponding to MyoG and a red signal corresponding to MHC were observed, with approximately 90% overlap.
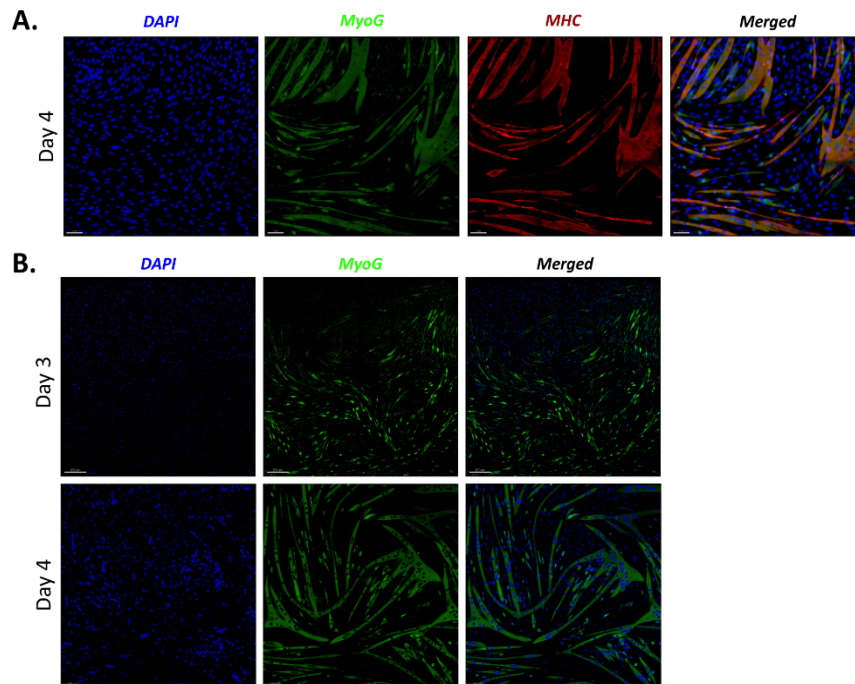
Figure 10: Unpatterned C2C12 Differentiation Immunofluorescence Assay; (A.) Cells (passage 8-12) fixed on Day 4 of differentiation, stained for MyoG and MHC markers. (B.) Cells fixed on Day 3 (passage 16-20) and 4 (passage 8-12) of differentiation, stained for MyoG marker. (Images shown are stitched tile-scans taken at 40x)

As shown in **Figure 10B.**; upon staining the C2C12 cells (passage number between 16 to 20) on Day 3 of differentiation for MyoG, the green signal was predominantly observed within nuclei. Whereas, for the cells (passage number between 8 to 12) stained for MyoG on Day 4 of differentiation, the green signal was only seen in the cytoplasm and not in the nuclei.

3.3. ALIGNED C2C12 DIFFERENTIATION

ECM proteins were micropatterned into line patterns of various widths and spacing to possibly direct aligned differentiation of C2C12 myoblasts confined within the lines. Upon differentiation, the cells were stained for MHC and the immunofluorescence images were captured.

3.3.1. Pilot Patterning Experiments

The immunofluorescence images of the pilot 96 square-well patterning experiments are summarized in **Figure 11A.** Line patterns of spacing 15 µm, 30 µm, 60 µm, 90 µm and 120 µm across 30 µm, 60 µm and 90 µm widths were tested. Preferentially aligned myotubes, deviating from the direction of the line patterns were observed in both 30 µm and 60 µm line widths, across all the line spacings. The myotubes were observed to bridge between the lines and did not show confinement within the patterned areas. This bridging of the myotubes was also noted to be preferential towards the right of the line patterns. Similar observations were seen in the 90 µm line width, but the alignment of the myotubes was not as ordered in comparison to the 30 µm and 60 µm line widths.
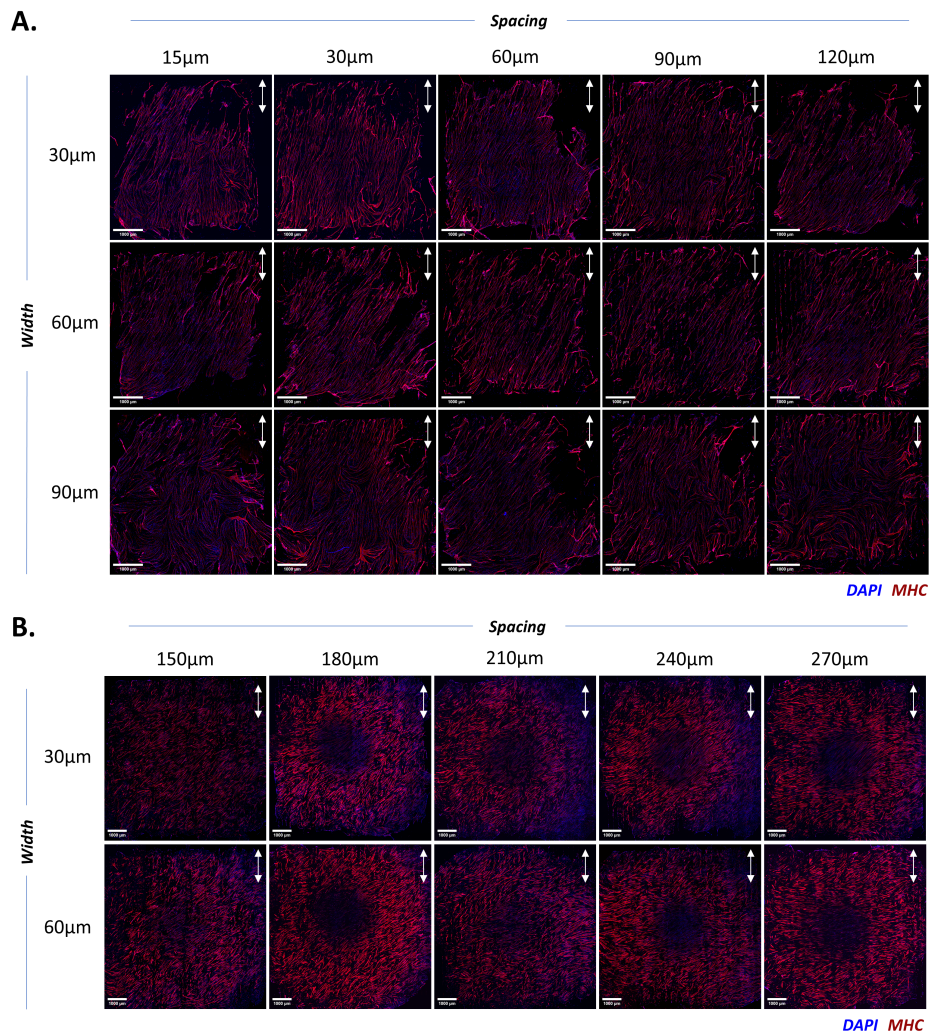
Figure 11: Immunofluorescence assay of C2C12 differentiation on line-patterns of increasing width and spacing; (A.) 96 square-well pilot, (B.) 24 circular-well pilot. Double-headed white arrows indicate the direction of the lines. (Images shown are stitched tile-scans taken at 10x)

A new pilot patterning experiment was performed with the 24 circular-well plate, with line patterns of increased spacing of 150 µm, 180 µm, 210 µm, 240 µm and 270 µm, across 30 µm and 60 µm widths respectively. The immunofluorescence images of the differentiated C2C12 cells from the above experiment are summarized in **Figure 11B.** Like the 96 well patterning experiment, the myotubes displayed preferentially alignment with rightward deviation. The myotubes still showed bridging, even across the lines of increased spacings. Looking closely, the myotube elongation appeared to be subpar in comparison to the 96 well experiment and the cells were overcrowded.

3.3.2. Optimized Patterning Experiment

The immunofluorescence images of the differentiated C2C12 cells from the optimized 24 circular-well patterning experiment are shown in **Figure 12.** Interestingly, the differentiating myotubes appeared to have detached in most of the patterned wells. Bridging of myotubes across the lines was still observed, as seen in the pattern of 270 µm spacing. Moreover, the cells were observed to detach as cell-sheets during the staining protocol, as illustrated in the 240 µm line spacing images (**Figure 12.**, outlined by yellow dashed lines).
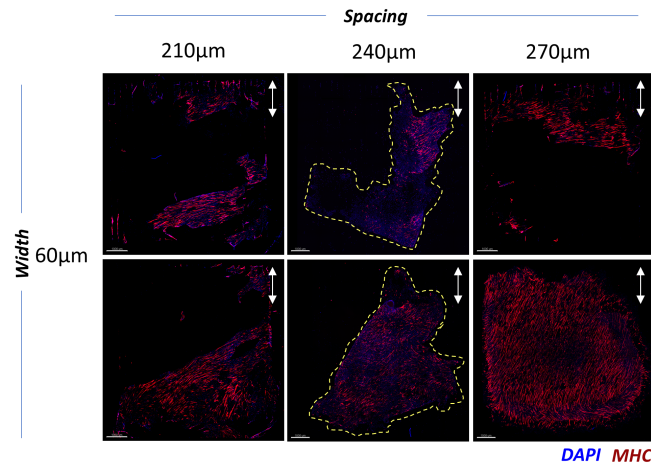
Figure 12: Immunofluorescence assay of C2C12 differentiation from the optimized 24 circular-well patterning experiment. Double-headed white arrows indicate the direction of the lines. Yellow dashed-lines outline the detaching cell-sheets. (Images shown are stitched tile-scans taken at 10x)

3.3.3. Pattern Validation

The micropatterned wells set aside for validation from the pilot and optimized patterning experiments were stained with Alexa-647 secondary antibody to visualize the patterning quality of the line patterns. **Figure 13A.** visualizes the quality of some of the patterns from the pilot experiments and clear imperfections were observed. Irregular ring-like structures were present in the patterns (**Figure 13 ai, aii & aiii.**) and when observed closely, particle artefacts bridging the lines were also recorded (**Figure 13 aiii.**). Conversely, in **Figure 13B.** which illustrates the patterns from the optimizing patterning experiments, a marked difference in quality was observed. Only minor ring imperfections were observed, but overall, no bridging artefacts were seen between the lines.
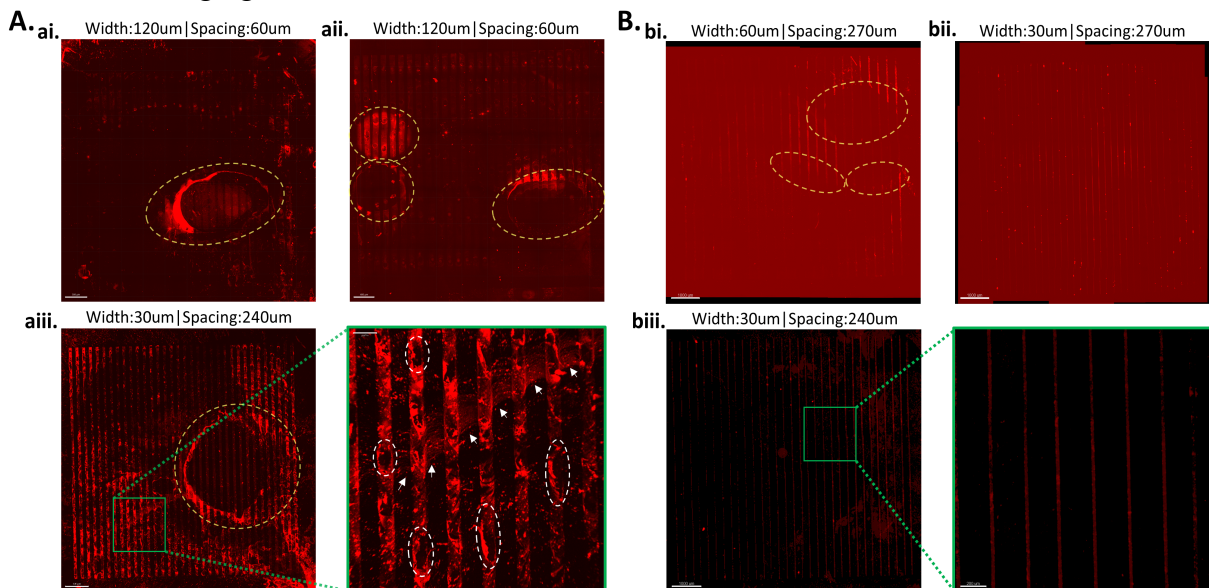
Figure 13: Validation of Patterns: (A.) Pilot patterning experiment and (B.) Optimized patterning experiment. Yellow circles mark the ring-like imperfections and white arrows indicate the particle artefacts between the lines. (Images shown are stitched tile-scans taken at 10x)

The important difference in the protocol between the pilot and optimized experiments was that the PLPP gel was prepared with Triton X-100 diluted in PBS in the former and with MQ water in the latter experiment.

3.3.4. Orientation Analysis

The alignment of the differentiated myotubes from the patterning experiments was quantified using the AFT and OrientationJ tools. These tools were used to generate the orientation colour maps from the processed binary image of the MHC channel (summarized in **Figure 14**). The colour maps generated by both tools appeared closely similar. The Dominant Direction function of the OrientationJ plugin was also used to determine the major orientation direction of the myotubes in an image. The major orientation direction was then used to calculate the deviation angle (shown in **Figure 14**) of the myotube alignment with respect to the line patterns.
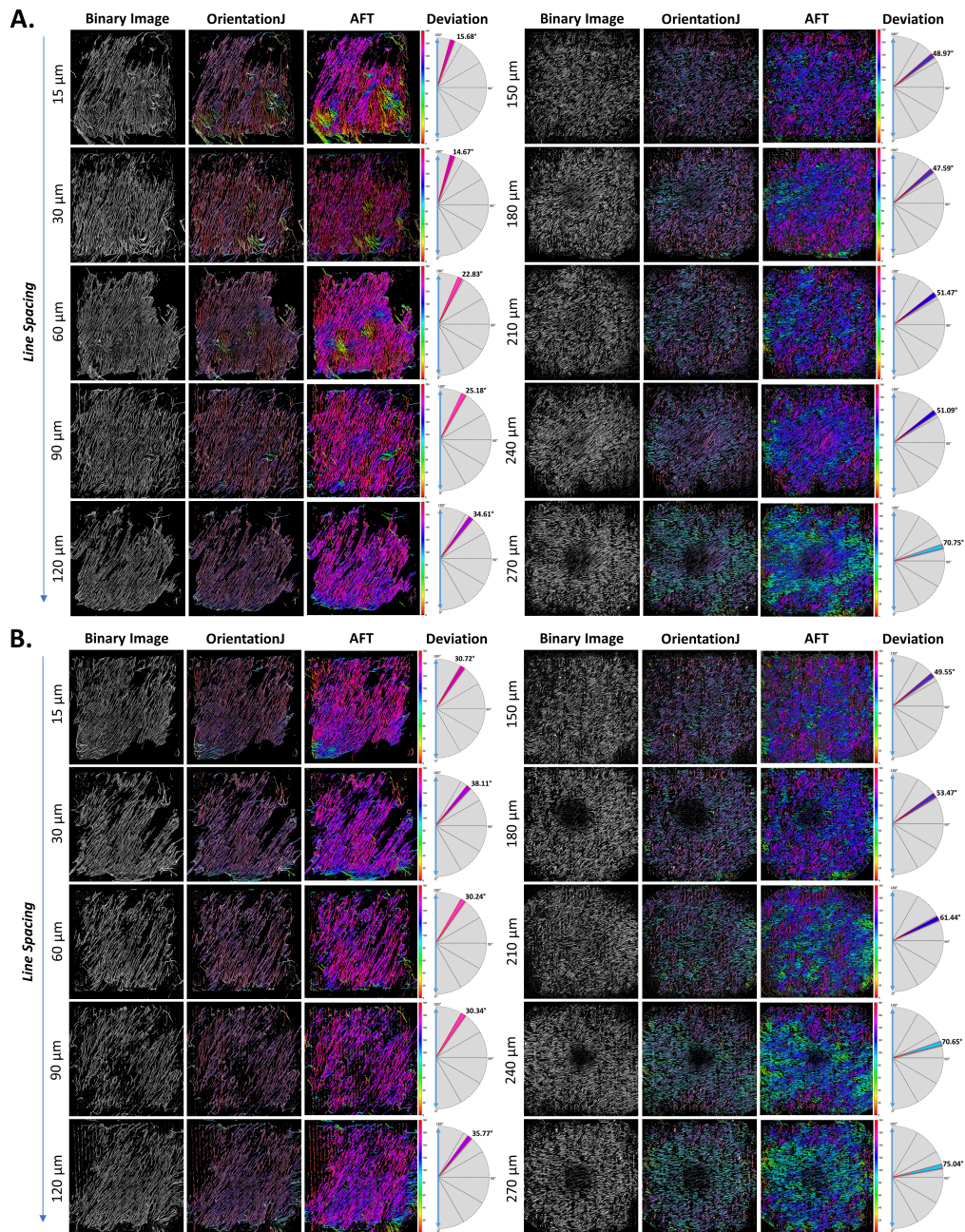
Figure 14: Orientation analysis of the line-patterned C2C12 myotubes: (i) Binary images of the MHC channel, (ii) Orientation colour maps from OrientationJ and AFT (in HSB colour space), (iii) Deviation angle of the myotube alignment with respect to the direction of line-patterns of (A.) 30 μm and (B.) 60 μm widths of increasing spacing (15 – 270 μm).

A preferential alignment of the myotubes with a rightward bias was evident from the orientation colour maps of all the line patterns of both 30 μm (**Figure 14A.**) and 60 μm (**Figure 14B.**) widths of increasing spacing. Interestingly, the rightward deviation bias of the alignment was observed to increase with the increase in line spacing of both 30 μm and 60 μm line widths, as illustrated in **Figure 15B.**
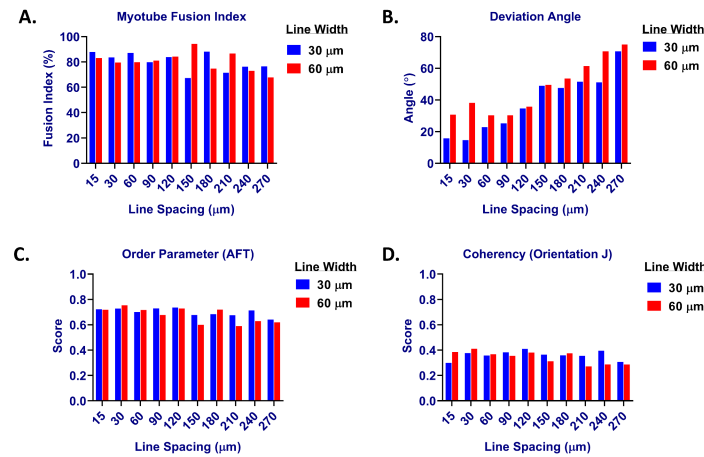
Figure 15: C2C12 differentiation analysis on line patterns of 30 μm and 60 μm widths of increasing spacing; (A.) Myotube fusion index calculated using the nuclei count obtained from the DAPI and MHC channel binary images, (B.) Deviation angle of the aligned myotubes from the line-pattern direction calculated using OrientationJ (Dominant direction) plugin, (C.) Order parameter score (0 = isotropic, 1 = anisotropic) of the myotube alignment generated by the AFT tool, (D.) Coherency score (0 = isotropic, 1 = anisotropic) of the myotube alignment generated by the OrientationJ (Dominant direction) plugin.

The quality of the C2C12 differentiation output from the patterning experiments was determined by calculating the myotube fusion index. This was done by calculating the ratio of the number of nuclei present inside the myotubes in relation to the total number of nuclei, from the binary images of both DAPI and MHC channels. The myotube fusion index was similar across the different patterns, with an average of over 75-80% (**Figure 15A.**)

Both the AFT and OrientationJ tools generated an alignment score based on the isotropy of the myotubes in the binary images, labelled as Order Parameter and Coherency respectively. An image with fully isotropic objects is given a score of 0, while a fully anisotropic image is given a score of 1. The average Order Parameter across all the patterns was approximately 0.7 (**Figure 15C.**). Whereas, the average Coherency was approximately 0.35 (**Figure 15D.**) for the same images.

4.1. MESODERM DIFFERENTIATION

4.1.1. Differentiation Protocol 1 (Chal et.al)

The SM differentiation protocol published by Chal et.al was used to direct paraxial mesoderm induction of the double reporter (MSGN1-mCherry & PAX3-Venus) hiPSCs. The above protocol suggested a 3mg/ml Matrigel coating concentration for setting up the differentiation. However, this seemed to be very high in comparison to a similar study that reported a 1:50 Matrigel dilution (0.2 – 0.4 mg/ml, depending on the LOT No.) to induce mesoderm differentiation (70,71).

The differentiation progress of the hiPSCs seeded at 9.5×10^4 cells on four Matrigel concentrations (0.11, 0.22, 0.44 & 0.66 mg/ml) was recorded to compare the differentiation outputs. Although there were qualitative differences in colony morphologies between the Matrigel concentrations, the mCherry signal corresponding to MSGN1 expression was unanimously recorded on Day 4 (**Figure 7A.**). Moreover, the differences in the relative expression levels of the mesodermal markers on Day 5 were negligible between the Matrigel concentrations (**Figure 7B.**). From this pilot experiment, 0.22 mg/ml of Matrigel concentration appeared to be likely sufficient to execute mesodermal induction. However, the 9.5×10^4 starting cell number was low and was increased in the later experiment. The results of the differentiation performed using 1.25×10^5 cells on 0.22 mg/ml Matrigel, showed the expressions levels of MSGN1, Tbx6 and TbxT went down from Day 3 onwards, while PAX3 expression went up significantly (**Figure 7C.**). However, it is difficult to comment on the expression profiles, as the levels were not recorded on Days 1 and 2 of the differentiation. The 1.25×10^5 starting cell number also appeared to be insufficient, as most colonies started to detach by Day 4.

4.1.2. Differentiation Protocol 2 (Cao et.al)

The mesoderm differentiation protocol published by Cao et.al was tested on two hiPSC lines (LUMC30CL12 & LUMC31CL08) seeded at different starting cell numbers. The differentiation progress was only recorded qualitatively by capturing brightfield images on each day of differentiation. Only the 300K starting cell number of the LUMC30CL12 line (**Figure 8A.**) showed progressive growth of the embryoid-like bodies, while the growth of the LUMC31CL08 line (**Figure 8B.**) plateaued by Day 2. However, this observation can be linked to differences in the cell densities between the two hiPSC lines on Day 0, even though the starting cell number was identical. This discrepancy could likely be due to a cell counting error between the two hiPSC lines. This means that we cannot be certain to compare the differentiation results of the two hiPSC lines.

The mesoderm differentiation experiments performed in this study were very limited and the data was not sufficient to make any conclusive comments on the differentiation output. The results of these limited experiments cannot be taken as evidence to make any conclusions on the efficacy of the differentiation protocols that were tested in this study.

4.2. C2C12 DIFFERENTIATION

The C2C12 differentiation protocol was validated by quantifying the relative expression levels of the myogenic markers on different days of differentiation using RT-qPCR. The expression levels of the myoblast determination markers, Myf5 and MyoD, were observed to downregulate as the protocol progressed. Whereas the terminal myogenic differentiation markers, MyoG and Myh1, were well upregulated as expected (**Figure 9B.**).
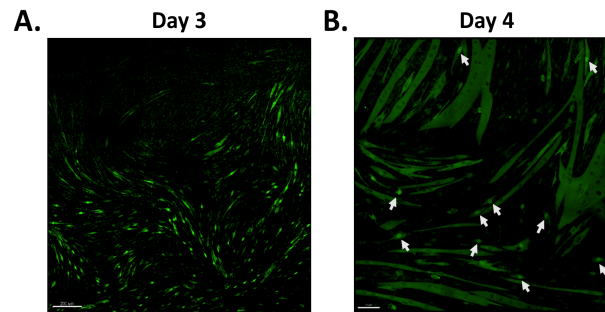
Figure 16: **MyoG localization during C2C12 Differentiation Immunofluorescence Assay;** (A.) Day 3 of differentiation (passage 16-20) (B.) Day 4 of differentiation (passage 8-12). White arrows mark cells with nuclear MyoG signal (Images shown are stitched tile-scans taken at 40x)

Additionally, immunofluorescence microscopy was used to validate the differentiation of C2C12 myoblasts by staining for the late myogenic markers MyoG and MHC. On Day 4 of differentiation, MyoG and MHC signals were observed with almost 90% overlap (**Figure 9A.**). To further investigate the localization of MyoG, C2C12 myoblasts of a late passage number (16 to 20) were allowed to differentiate for 3 days and stained for MyoG. Interestingly, the MyoG signal was predominantly localized in the nuclei of the unfused myocytes in the early phase of differentiation (**Figure 16A.**). Whereas, when these myocytes fused to form myotubes, the MyoG diffused into the cytoplasm with no signal in the nuclei (**Figure 16B.**). Notably, the MyoG signal was still seen in the nuclei of the unfused single-celled myocytes on Day 4 of differentiation (**Figure 16B.**, shown by white arrows).

4.3. ALIGNED C2C12 DIFFERENTIATION

Line patterns of various widths and spacings were created by photopatterning ECM proteins to possibly guide aligned differentiation of the C2C12 myoblasts. It was hypothesized that the differentiating myotubes would align along the line patterns in a vertical fashion. Interestingly, the results showed that the myotubes indeed demonstrated alignment, but with the orientation deviating rightwards away from the line pattern direction.

4.3.1. Rightward Orientation Bias

The angle of the rightward orientation bias of the myotube alignment was seen to increase with the increase in spacing between the lines (**Figure 15B.**). Similar observations were recorded in previous studies that explored the alignment of C2C12 myotubes when differentiated on line patterned substrates (43,49). The study by RM Duffy et.al attempted to guide alignment by microcontact stamping of ECM proteins in line patterns of various widths and spacings. While the study by SD Cakal et.al 3D printed lines of gelatin micro-ridges to guide alignment. In both the above studies, the C2C12 myotubes were recorded to align with a rightward orientation bias, as observed in our study. The authors of either study acknowledge the bias in alignment, but do not explain the reason for this observation.

A possible explanation could be that the myotubes attempt to maximize their contact area of attachment by aligning along the longer diagonal axis of the patterned regions. However, this does not explain the orientation bias of the myotubes being preferential only to the right. On further investigation, it was found that biological cells intrinsically exhibit chirality and left-right asymmetry (72). A study by LQ Wan et.al extensively explored the preferential orientation bias of various cell phenotypes on a micropatterned substrate in different treatment conditions. Myoblasts were reported to have an opposite orient bias in comparison to other cell types and inhibition of actin reversed the orientation bias. The above study showed that the orientation bias is cell phenotype dependent and linked to the actin cytoskeleton function (73). This likely explains the preferential rightward deviation of the C2C12 myotubes observed in our study.

4.3.2. Lack of Myotube Confinement

The C2C12 myotubes from the patterning experiments were seen to bridge across the line patterns and lacked confinement within the patterned regions (**Figure 11**). When observing the images from the pilot 96 square-well patterning experiment (**Figure 11A.**), we initially attributed the cell bridging to the close spacing of the lines. However, the cell bridging was still evident in the 24 circular-well patterning experiment with increased line spacings as well (**Figure 11B.**)

The pattern validation experiments revealed that the patterning quality of either experiment was sub-optimal (**Figure 13A.**). It was later found that the 2% PLPP gel used for the coating was prepared using 0.1% Triton X-100 diluted in PBS instead of MQ water. The PBS crystals that precipitated during the evaporation step likely interfered with the gel distribution (**Figure 13 ai & aii.**). The uneven gel combined with the PBS precipitates mostly likely interfered with the UV laser during patterning. This possibly created particulate artefacts that bridged the line patterns (**Figure 13 aiii.**) and caused sub-optimal patterns as a result.

The 24 circular-well patterning experiment was repeated with an optimized coating protocol, with a clean 2% PLPP gel prepared using 0.1% Triton X-100 diluted in MQ water. Upon validation, the patterning quality was markedly better (**Figure 13B.**) in the latest patterning experiment using the optimized protocol. Despite the optimal patterning quality, the myotubes still bridged across the lines and notably detached upon differentiation (**Figure 12.**). The detachment of the myotubes was a new observation and was not observed in any of the patterned wells in the pilot experiments (**Figure 11**). The observed cell bridging was likely a result of high initial cell density, and upon differentiation the pulling forces of the myotubes caused the cell sheets to detach. Unlike the optimized patterning experiment, the sub-optimal patterning in the pilot experiments likely resulted in an increased overall patterned surface area for the cells to attach. This is a likely explanation for the myotubes from the pilot experiments to have remained adherent upon differentiation.

4.3.3. Image Binarization

The immunofluorescent images of the patterning experiments were processed in Fiji to convert them into binarized images. The image processing protocol used in our study was developed based on a method published by Xu et.al (61). When the method published in the above study was implemented without any modifications to our images, the achieved output

was sub-par to what was expected. The thresholding method suggested in the study was not suitable for our images.

Thresholding is the crucial step that converts an image to quantifiable binary data by separating the objects of interest from the background. Most images vary from each other due to variables like colour, brightness, background fluorescence and shape of objects. This means that the thresholding method which might work well for one image, might not work for another. The *'Sauvola'* Auto Local Threshold method suggested by Xu et.al did not work optimally for our images. Instead, the *'Phansalkar'* method proved to work very well to binarize the myotube (MHC) channel of our images. However, the same method did not work for the nucleus (DAPI) channel, rather the *'Default'* Auto Threshold method worked.

Given the above condition, it is important to note that the binarization protocol suggested in our study might need minor optimizations to work flawlessly on other immunofluorescence images with different channel colours or brightness inhomogeneity.

4.3.4. Orientation Analysis Tools

The alignment of the myotubes from the patterning experiments was analyzed using the AFT and OrientationJ tools. Both tools implement a grid-based 2D FFT method to scan a binary image in small windows to map out a vector field corresponding to the orientation of the objects. This vector field is then used to quantify the orientation of the objects in the image and a corresponding orientation colour map is generated.

In our study, both tools were compared against each other in terms of accuracy, sensitivity, functionality and user control. It was ensured that matching parameters were used to run both tools. The 'Window Size' (AFT) and 'Local Window' (OrientationJ) were set to '10 pixels', with 'Overlap' (AFT) and 'Grid Size' (OrientationJ) set to '50' for both tools respectively. However, the AFT tool provided additional input parameters like, 'Neighbourhood Radius' which was set to '2' and 'Local Filtering' to filter out blank spaces in the image. The above parameters were used to generate an orientation colour map and an alignment score for the myotube binary images. Additionally, the 'Dominant Direction' function of the OrientationJ tool was used to determine the major orientation angle of the myotubes in an image, which was then used to calculate the deviation angle.
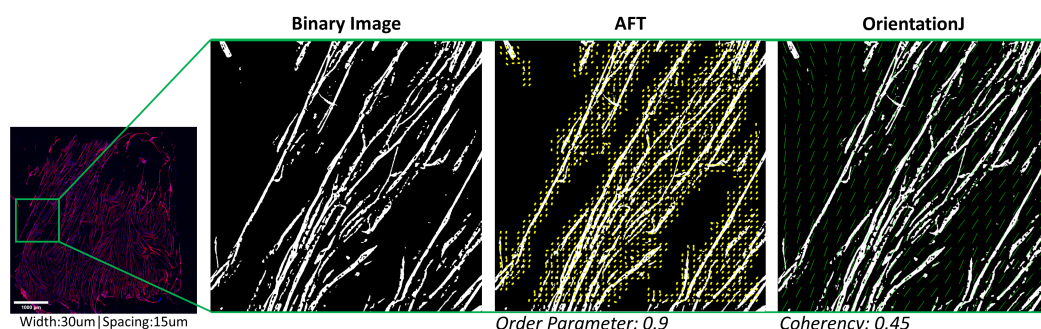
Figure 17: Comparison of orientation vector maps generated by AFT and OrientationJ for cropped in myotube binary image. (AFT parameters – Window Size: '40 px', Overlap: '50%', Neighbourhood Radius: '2', Filter Blank Regions 'Yes'. OrientationJ parameters – Local Window: '40 px', Grid Size: '50')

The orientation colour maps generated by both tools were closely comparable, with no noticeable differences (**Figure 14**). However, there was a big difference between the alignment scores generated by both tools (**Figure 15C. & 15D.**). The average score generated

by OrientationJ was approximately half the average score generated by AFT for the same images. To investigate this, vector maps were generated using both tools for a cropped binary image of one of the patterned myotubes (**Figure 17**). Taking a closer look at the vector fields, it was evident that AFT filters out the blank regions and does not include them in the final mapping, while OrientationJ maps out the blank regions as well. This most likely explains the alignment score of OrientationJ being half of AFT's score.

The AFT tool demonstrated to be superior to OrientationJ with respect to isolating the myotubes from the background and generating an accurate alignment score. Furthermore, AFT provided additional user-adjustable parameters, which allowed for more flexibility to improve the sensitivity of orientation analysis. On the other hand, OrientationJ had more quantitative functionality, with the ability to generate a numerical orientation distribution that can be plotted. While AFT was limited to orientation colour maps and alignment scores only.

CONCLUSIONS AND REMARKS

The first part of our study focused on paraxial mesoderm differentiation of hiPSCs *in-vitro*. The paraxial mesoderm induction of hiPSCs using the directed differentiation protocol published by Chal et.al was successfully validated. The expression of the mesodermal markers MSGN1, Tbx6 and TbxT was confirmed using RT-qPCR. Additionally, MSGN1 expression was also confirmed by the corresponding mCherry fluorescence from the hiPSC reporter line. However, the results from mesoderm differentiation performed using the protocol published by Cao et.al were inconclusive and not sufficient to make any remarks. From the limited experiments, we learned that optimal Matrigel concentrations and starting cell numbers are crucial for successful *in-vitro* differentiation of hiPSCs. A comprehensive comparison of the mesodermal differentiation efficacy between the two protocols can be made in the future by using a common hiPSC line and starting cell number.

The second major part of our study focused on directing aligned *in-vitro* differentiation of C2C12 myoblasts using photopatterning. The differentiation protocol was successfully validated by quantifying the expression of relevant myogenic markers using RT-qPCR and immunofluorescence assay. It was initially hypothesized that the differentiated myotubes would align vertically along the parallel line patterns that were created by photopatterning of ECM proteins. However, from the pilot experiments, we were able to conclude that the myotubes preferentially aligned with a rightward orientation bias deviating from the line patterns. Moreover, the angle of the rightward bias demonstrated by the myotubes increased with the increase in spacing between the lines. Furthermore, the quality of differentiation in the pilot patterning experiments was very good with an average myotube fusion index of over 75-80%. It is important to note that the patterning experiments were limited and the repeatability of the above results will need to be validated in future studies.

The image processing protocol developed in this study worked successfully in binarizing the immunofluorescence images of the differentiated C2C12 myotubes for orientation analysis. The comparison between AFT and OrientationJ orientation analysis tools revealed that each tool has its advantages and limitations. According to our study, AFT was superior at filtering blank regions, accurately mapping the myotubes and providing more controllable analysis parameters. On the other hand, OrientationJ outperformed AFT in providing diverse quantitative functionalities, including numerical orientation distribution and plottable orientation data.

The preferential rightward orientation bias exhibited by the C2C12 myoblasts is a potential characteristic that could be worth exploring in future research. Understanding this preferential bias could be relevant to designing 3D scaffolds, that either compensate for the bias or utilize it to better mimic the organization of the native SM tissue. Additionally, the micropattern designs and seeding density of the C2C12 myoblasts must be optimized in future photopatterning experiments to improve the confinement of the differentiating myotubes. Generating aligned myotubes that are confined to pre-defined geometries and orientations is crucial for developing a platform that can be used to validate alignment quantification tools. The long-term goal is to apply this platform to train a machine learning algorithm that can fully automate the orientation analysis of SM cells in both 2D and 3D culture systems.

6.1. RT-QPCR ANALYSIS

Table 4A: Primer sequences used to set up the qPCR reactions

Gene	Forward Primer	Reverse Primer
GAPDH	TCACCACCATGGAGAAGGC	GCTAAGCAGTTGGTGGTGCA
MSGN1	AACCTGCGCGAGACTTTCC	ACAGCTGGACAGGGAGAAGA
Tbx6	CATCCACGAGAATTGTACCCG	AGCAATCCAGTTTAGGGGTGT
TbxT	CCTCGTTCTGATAAGCAGTCAC	TATGAGCCTCGAATCCACATAGT
PAX3	TGCCGTCAGTGAGTTCCATCAGC	GCTAAACCAGACCTGTACTCGGGC
Myf5	AAGGCTCCTGTATCCCCTCAC	TGACCTTCTTCAGGCGTCTAC
MyoD	GAGCGCATCTCCACAGACAG	AAATCGCATTGGGGTTTGAG
MyoG	GCAGGCTCAAGAAAGTGAATG	CACTTAAAAGCCCCCTGCTAC
Myh1	CTTCAACCACCACATGTTCG	AGGTTTGGGCTTTTGGAAGT

6.2. IMAGE PROCESSING AND ANALYSIS

6.2.1. Image Binarization

Table 5A: Fiji macros of DAPI and MHC channel binarization

DAPI Binarization Macro	MHC Binarization Macro
run("Despeckle"); *setOption("ScaleConversions", true);* *run("8-bit");* *run("Auto Threshold", "method=Default ignore_black white");* *run("Options...", "iterations=1 count=1 black do=Nothing");* *setOption("BlackBackground", true);* *run("Convert to Mask");*	*run("Despeckle");* *setOption("ScaleConversions", true);* *run("8-bit");* *run("Auto Local Threshold", "method=Phansalkar radius=15 parameter_1=0 parameter_2=0 white");* *run("Open");* *run("Options...", "iterations=1 count=1 black do=Nothing");* *setOption("BlackBackground", true);* *run("Convert to Mask");*

6.2.2. Myotube Fusion Index

Table 6A: Fiji macro for analysing particles to count nuclei

Processing Steps – Particle Analysis

```
list = getList("image.titles");


for(i = 0;i<list.length;i++){

        if(matches(list[i],".*DAPI.tif*")){

                selectWindow(list[i]);

                }

}
setOption("BlackBackground", true);

run("Dilate");

run("Watershed");


list = getList("image.titles");


for(i = 0;i<list.length;i++){

        if(matches(list[i],".*MHC.tif*")){

                selectWindow(list[i]);

                }

}
run("Dilate");

run("Images to Stack", "use keep");

run("Z Project...", "projection=[Max Intensity]");

selectWindow("Stack");

close();

run("Analyze Particles...", "size=30-300 summarize");

list = getList("image.titles");


for(i = 0;i<list.length;i++){

        if(matches(list[i],".*DAPI.tif*")){

                selectWindow(list[i]);

                }

}
```

```
run("Analyze Particles...", "size=30-300 summarize");

list = getList("image.titles");


for(i = 0;i<list.length;i++){

        if(matches(list[i],".*MHC.tif*")){

                selectWindow(list[i]);

                }

}
run("Analyze Particles...", "size=30-300 summarize");

close();

close();

selectWindow("MAX_Stack");

close();
```

6.3. MESODERM DIFFERENTIATION

6.3.1. Differentiation Protocol 2 (Cao et.al)
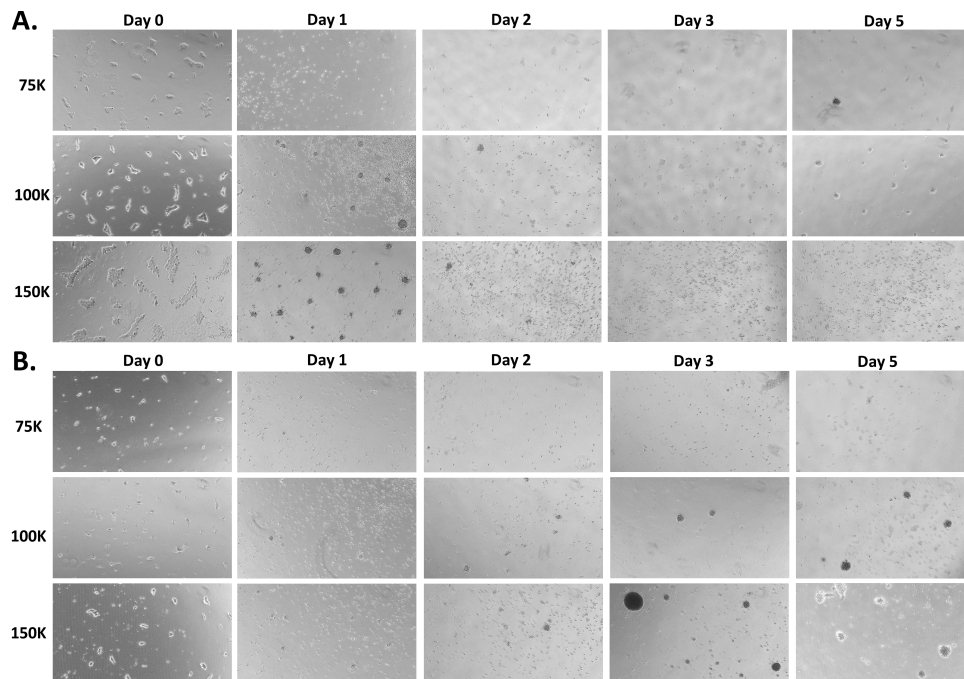
Figure 18A: Mesoderm Differentiation Cao. et.al Protocol; Brightfield images of the hiPSCs differentiation progression taken on Days 0, 1, 2, 3 & 5 for the different starting cell numbers of (A.) LUMC30CL12 & (B.) LUMC31CL08 hiPSC lines (images taken at 4x).

6.4. C2C12 DIFFERENTIATION

6.4.1. RT-qPCR Statistical Tests

Table 7A: Ordinary One-way ANOVA - Myf5

Tukey's multiple comparisons test	Mean Diff.	95.00% CI of diff.	Significant?	Summary	Adjusted P Value
Day 0 vs. Day 1	-0.5260	-0.6955 to -0.3565	Yes	****	<0.0001
Day 0 vs. Day 2	-0.1114	-0.2809 to 0.05805	No	ns	0.4916
Day 0 vs. Day 3	0.4564	0.2759 to 0.6368	Yes	****	<0.0001
Day 0 vs. Day 4	0.5031	0.3336 to 0.6726	Yes	****	<0.0001
Day 0 vs. Day 5	0.5646	0.3951 to 0.7341	Yes	****	<0.0001
Day 0 vs. Day 6	0.7432	0.5737 to 0.9127	Yes	****	<0.0001
Day 0 vs. Day 7	0.7039	0.5344 to 0.8734	Yes	****	<0.0001
Day 0 vs. Day 8	0.7710	0.6015 to 0.9405	Yes	****	<0.0001
Day 1 vs. Day 2	0.4146	0.2189 to 0.6103	Yes	****	<0.0001
Day 1 vs. Day 3	0.9824	0.7771 to 1.188	Yes	****	<0.0001
Day 1 vs. Day 4	1.029	0.8334 to 1.225	Yes	****	<0.0001
Day 1 vs. Day 5	1.091	0.8949 to 1.286	Yes	****	<0.0001
Day 1 vs. Day 6	1.269	1.074 to 1.465	Yes	****	<0.0001
Day 1 vs. Day 7	1.230	1.034 to 1.426	Yes	****	<0.0001
Day 1 vs. Day 8	1.297	1.101 to 1.493	Yes	****	<0.0001
Day 2 vs. Day 3	0.5678	0.3626 to 0.7731	Yes	****	<0.0001
Day 2 vs. Day 4	0.6146	0.4188 to 0.8103	Yes	****	<0.0001
Day 2 vs. Day 5	0.6760	0.4803 to 0.8717	Yes	****	<0.0001
Day 2 vs. Day 6	0.8546	0.6589 to 1.050	Yes	****	<0.0001
Day 2 vs. Day 7	0.8153	0.6196 to 1.011	Yes	****	<0.0001
Day 2 vs. Day 8	0.8825	0.6867 to 1.078	Yes	****	<0.0001
Day 3 vs. Day 4	0.04673	-0.1585 to 0.2520	No	ns	0.9984
Day 3 vs. Day 5	0.1082	-0.09707 to 0.3135	No	ns	0.7642
Day 3 vs. Day 6	0.2868	0.08154 to 0.4921	Yes	***	0.0008
Day 3 vs. Day 7	0.2475	0.04224 to 0.4528	Yes	**	0.0067
Day 3 vs. Day 8	0.3146	0.1094 to 0.5199	Yes	***	0.0001
Day 4 vs. Day 5	0.06147	-0.1342 to 0.2572	No	ns	0.9857
Day 4 vs. Day 6	0.2401	0.04436 to 0.4358	Yes	**	0.0054
Day 4 vs. Day 7	0.2008	0.005067 to 0.3965	Yes	*	0.0397
Day 4 vs. Day 8	0.2679	0.07219 to 0.4636	Yes	**	0.0011
Day 5 vs. Day 6	0.1786	-0.01711 to 0.3743	No	ns	0.1030
Day 5 vs. Day 7	0.1393	-0.05640 to 0.3350	No	ns	0.3799
Day 5 vs. Day 8	0.2064	0.01072 to 0.4022	Yes	*	0.0305

	Mean Diff.	95.00% CI of diff.	Significant?	Summary	Adjusted P Value
Day 6 vs. Day 7	-0.03929	-0.2350 to 0.1564	No	ns	0.9994
Day 6 vs. Day 8	0.02783	-0.1679 to 0.2235	No	ns	>0.9999
Day 7 vs. Day 8	0.06712	-0.1286 to 0.2628	No	ns	0.9752

Table 8A: Ordinary One-way ANOVA - MyoD

Tukey's multiple comparisons test	Mean Diff.	95.00% CI of diff.	Signific-ant?	Sum-mary	Adjusted P Value
Day 0 vs. Day 1	0.4028	0.09216 to 0.7134	Yes	**	0.0025
Day 0 vs. Day 2	0.08400	-0.2266 to 0.3946	No	ns	0.9947
Day 0 vs. Day 3	-0.2918	-0.6225 to 0.03892	No	ns	0.1296
Day 0 vs. Day 4	-0.6157	-0.9263 to -0.3051	Yes	****	<0.0001
Day 0 vs. Day 5	-0.8654	-1.176 to -0.5548	Yes	****	<0.0001
Day 0 vs. Day 6	-0.8270	-1.138 to -0.5164	Yes	****	<0.0001
Day 0 vs. Day 7	-0.8560	-1.167 to -0.5454	Yes	****	<0.0001
Day 0 vs. Day 8	-1.207	-1.518 to -0.8968	Yes	****	<0.0001
Day 1 vs. Day 2	-0.3188	-0.6775 to 0.03989	No	ns	0.1235
Day 1 vs. Day 3	-0.6946	-1.071 to -0.3184	Yes	****	<0.0001
Day 1 vs. Day 4	-1.018	-1.377 to -0.6598	Yes	****	<0.0001
Day 1 vs. Day 5	-1.268	-1.627 to -0.9095	Yes	****	<0.0001
Day 1 vs. Day 6	-1.230	-1.588 to -0.8711	Yes	****	<0.0001
Day 1 vs. Day 7	-1.259	-1.617 to -0.9001	Yes	****	<0.0001
Day 1 vs. Day 8	-1.610	-1.969 to -1.252	Yes	****	<0.0001
Day 2 vs. Day 3	-0.3758	-0.7520 to 0.0004210	No	ns	0.0505
Day 2 vs. Day 4	-0.6997	-1.058 to -0.3410	Yes	****	<0.0001
Day 2 vs. Day 5	-0.9494	-1.308 to -0.5907	Yes	****	<0.0001
Day 2 vs. Day 6	-0.9110	-1.270 to -0.5523	Yes	****	<0.0001
Day 2 vs. Day 7	-0.9400	-1.299 to -0.5813	Yes	****	<0.0001
Day 2 vs. Day 8	-1.291	-1.650 to -0.9328	Yes	****	<0.0001
Day 3 vs. Day 4	-0.3239	-0.7001 to 0.05227	No	ns	0.1513
Day 3 vs. Day 5	-0.5736	-0.9498 to -0.1974	Yes	***	0.0002
Day 3 vs. Day 6	-0.5352	-0.9114 to -0.1591	Yes	***	0.0006
Day 3 vs. Day 7	-0.5642	-0.9404 to -0.1880	Yes	***	0.0002
Day 3 vs. Day 8	-0.9157	-1.292 to -0.5395	Yes	****	<0.0001
Day 4 vs. Day 5	-0.2497	-0.6084 to 0.1090	No	ns	0.4109
Day 4 vs. Day 6	-0.2113	-0.5700 to 0.1474	No	ns	0.6391

Day 4 vs. Day 7	-0.2403	-0.5990 to 0.1184	No	ns	0.4651
Day 4 vs. Day 8	-0.5918	-0.9505 to -0.2331	Yes	****	<0.0001
Day 5 vs. Day 6	0.03838	-0.3203 to 0.3971	No	ns	>0.9999
Day 5 vs. Day 7	0.009405	-0.3493 to 0.3681	No	ns	>0.9999
Day 5 vs. Day 8	-0.3421	-0.7008 to 0.01661	No	ns	0.0741
Day 6 vs. Day 7	-0.02898	-0.3877 to 0.3297	No	ns	>0.9999
Day 6 vs. Day 8	-0.3805	-0.7391 to -0.02178	Yes	*	0.0288
Day 7 vs. Day 8	-0.3515	-0.7102 to 0.007202	No	ns	0.0595

Table 9A: Ordinary One-way ANOVA - MyoG

Tukey's multiple comparisons test	Mean Diff.	95.00% CI of diff.	Significant?	Summary	Adjusted P Value
Day 0 vs. Day 1	-671.2	-7844 to 6502	No	ns	>0.9999
Day 0 vs. Day 2	-2644	-9817 to 4529	No	ns	0.9617
Day 0 vs. Day 3	-15577	-23213 to -7941	Yes	****	<0.0001
Day 0 vs. Day 4	-26498	-33671 to -19325	Yes	****	<0.0001
Day 0 vs. Day 5	-23456	-30629 to -16283	Yes	****	<0.0001
Day 0 vs. Day 6	-12660	-19832 to -5487	Yes	****	<0.0001
Day 0 vs. Day 7	-10062	-17235 to -2889	Yes	***	0.0007
Day 0 vs. Day 8	-4217	-11390 to 2956	No	ns	0.6417
Day 1 vs. Day 2	-1973	-10255 to 6310	No	ns	0.9978
Day 1 vs. Day 3	-14905	-23592 to -6219	Yes	****	<0.0001
Day 1 vs. Day 4	-25827	-34109 to -17544	Yes	****	<0.0001
Day 1 vs. Day 5	-22785	-31067 to -14502	Yes	****	<0.0001
Day 1 vs. Day 6	-11989	-20271 to -3706	Yes	***	0.0004
Day 1 vs. Day 7	-9391	-17673 to -1108	Yes	*	0.0142
Day 1 vs. Day 8	-3546	-11828 to 4737	No	ns	0.9118
Day 2 vs. Day 3	-12933	-21619 to -4246	Yes	***	0.0002
Day 2 vs. Day 4	-23854	-32136 to -15572	Yes	****	<0.0001
Day 2 vs. Day 5	-20812	-29094 to -12530	Yes	****	<0.0001
Day 2 vs. Day 6	-10016	-18298 to -1734	Yes	**	0.0065
Day 2 vs. Day 7	-7418	-15701 to 864.2	No	ns	0.1173
Day 2 vs. Day 8	-1573	-9856 to 6709	No	ns	0.9996
Day 3 vs. Day 4	-10921	-19608 to -2235	Yes	**	0.0038
Day 3 vs. Day 5	-7879	-16566 to 807.5	No	ns	0.1075
Day 3 vs. Day 6	2917	-5770 to 11604	No	ns	0.9782
Day 3 vs. Day 7	5515	-3172 to 14201	No	ns	0.5404

Day 3 vs. Day 8	11360	2673 to 20046	Yes	**	0.0022
Day 4 vs. Day 5	3042	-5240 to 11324	No	ns	0.9625
Day 4 vs. Day 6	13838	5556 to 22120	Yes	****	<0.0001
Day 4 vs. Day 7	16436	8153 to 24718	Yes	****	<0.0001
Day 4 vs. Day 8	22281	13998 to 30563	Yes	****	<0.0001
Day 5 vs. Day 6	10796	2514 to 19078	Yes	**	0.0023
Day 5 vs. Day 7	13394	5111 to 21676	Yes	****	<0.0001
Day 5 vs. Day 8	19239	10956 to 27521	Yes	****	<0.0001
Day 6 vs. Day 7	2598	-5685 to 10880	No	ns	0.9858
Day 6 vs. Day 8	8443	160.4 to 16725	Yes	*	0.0421
Day 7 vs. Day 8	5845	-2437 to 14127	No	ns	0.3919

Table 10A: Ordinary One-way ANOVA – Myh1

Tukey's multiple comparisons test	Mean Diff.	95.00% CI of diff.	Significant?	Summary	Adjusted P Value
Day 0 vs. Day 1	-13.55	-5550 to 5523	No	ns	>0.9999
Day 0 vs. Day 2	-539.0	-6075 to 4998	No	ns	>0.9999
Day 0 vs. Day 3	-761.7	-6656 to 5132	No	ns	>0.9999
Day 0 vs. Day 4	-3155	-8692 to 2381	No	ns	0.6796
Day 0 vs. Day 5	-12786	-18323 to -7250	Yes	****	<0.0001
Day 0 vs. Day 6	-14572	-20109 to -9036	Yes	****	<0.0001
Day 0 vs. Day 7	-19880	-25417 to -14344	Yes	****	<0.0001
Day 0 vs. Day 8	-22731	-28268 to -17195	Yes	****	<0.0001
Day 1 vs. Day 2	-525.4	-6918 to 5868	No	ns	>0.9999
Day 1 vs. Day 3	-748.2	-7453 to 5957	No	ns	>0.9999
Day 1 vs. Day 4	-3142	-9535 to 3251	No	ns	0.8263
Day 1 vs. Day 5	-12773	-19166 to -6380	Yes	****	<0.0001
Day 1 vs. Day 6	-14559	-20952 to -8166	Yes	****	<0.0001
Day 1 vs. Day 7	-19867	-26260 to -13474	Yes	****	<0.0001
Day 1 vs. Day 8	-22718	-29111 to -16325	Yes	****	<0.0001
Day 2 vs. Day 3	-222.8	-6928 to 6482	No	ns	>0.9999
Day 2 vs. Day 4	-2616	-9009 to 3777	No	ns	0.9307
Day 2 vs. Day 5	-12247	-18640 to -5854	Yes	****	<0.0001
Day 2 vs. Day 6	-14033	-20426 to -7640	Yes	****	<0.0001
Day 2 vs. Day 7	-19341	-25734 to -12948	Yes	****	<0.0001
Day 2 vs. Day 8	-22192	-28585 to -15799	Yes	****	<0.0001
Day 3 vs. Day 4	-2394	-9099 to 4311	No	ns	0.9684

Day 3 vs. Day 5	-12025	-18730 to -5320	Yes	****	<0.0001
Day 3 vs. Day 6	-13811	-20516 to -7106	Yes	****	<0.0001
Day 3 vs. Day 7	-19119	-25824 to -12414	Yes	****	<0.0001
Day 3 vs. Day 8	-21970	-28675 to -15265	Yes	****	<0.0001
Day 4 vs. Day 5	-9631	-16024 to -3238	Yes	***	0.0002
Day 4 vs. Day 6	-11417	-17810 to -5024	Yes	****	<0.0001
Day 4 vs. Day 7	-16725	-23118 to -10332	Yes	****	<0.0001
Day 4 vs. Day 8	-19576	-25969 to -13183	Yes	****	<0.0001
Day 5 vs. Day 6	-1786	-8179 to 4607	No	ns	0.9934
Day 5 vs. Day 7	-7094	-13487 to -701.0	Yes	*	0.0180
Day 5 vs. Day 8	-9945	-16338 to -3552	Yes	***	0.0001
Day 6 vs. Day 7	-5308	-11701 to 1085	No	ns	0.1874
Day 6 vs. Day 8	-8159	-14552 to -1766	Yes	**	0.0031
Day 7 vs. Day 8	-2851	-9244 to 3542	No	ns	0.8911

REFERENCES

1. Frontera WR, Ochala J. Skeletal Muscle: A Brief Review of Structure and Function. Calcif Tissue Int. 2015 Mar;96(3):183–95.

2. Chal J, Pourquié O. Making muscle: skeletal myogenesis *in vivo* and *in vitro*. Development. 2017 Jun 15;144(12):2104–22.

3. Wang YX, Rudnicki MA. Satellite cells, the engines of muscle repair. Nat Rev Mol Cell Biol. 2012 Feb;13(2):127–33.

4. Relaix F, Zammit PS. Satellite cells are essential for skeletal muscle regeneration: the cell on the edge returns centre stage. Development. 2012 Aug 15;139(16):2845–56.

5. del Carmen Ortuño-Costela M, García-López M, Cerrada V, Gallardo ME. iPSCs: A powerful tool for skeletal muscle tissue engineering. Journal of Cellular and Molecular Medicine. 2019;23(6):3784–94.

6. Morgan J, Partridge T. Skeletal muscle in health and disease. Dis Model Mech. 2020 Feb 6;13(2):dmm042192.

7. Murphy M, Kardon G. Origin of Vertebrate Limb Muscle. In: Current Topics in Developmental Biology [Internet]. Elsevier; 2011 [cited 2022 Jun 17]. p. 1–32. Available from: https://linkinghub.elsevier.com/retrieve/pii/B9780123859402000012

8. Jiwlawat N, Lynch E, Jeffrey J, Van Dyke JM, Suzuki M. Current Progress and Challenges for Skeletal Muscle Differentiation from Human Pluripotent Stem Cells Using Transgene-Free Approaches. Stem Cells Int. 2018 Apr 11;2018:6241681.

9. Iberite F, Gruppioni E, Ricotti L. Skeletal muscle differentiation of human iPSCs meets bioengineering strategies: perspectives and challenges. npj Regen Med. 2022 Dec;7(1):23.

10. Park IH, Arora N, Huo H, Maherali N, Ahfeldt T, Shimamura A, et al. Disease-Specific Induced Pluripotent Stem Cells. Cell. 2008 Sep;134(5):877–86.

11. Maffioletti SM, Gerli MFM, Ragazzi M, Dastidar S, Benedetti S, Loperfido M, et al. Efficient derivation and inducible differentiation of expandable skeletal myogenic cells from human ES and patient-specific iPS cells. Nat Protoc. 2015 Jul;10(7):941–58.

12. Chal J, Al Tanoury Z, Hestin M, Gobert B, Aivio S, Hick A, et al. Generation of human muscle fibers and satellite-like cells from human pluripotent stem cells in vitro. Nat Protoc. 2016 Oct;11(10):1833–50.

13. Nogami K, Blanc M, Takemura F, Takeda S, Miyagoe-Suzuki Y, Nogami K, et al. Making Skeletal Muscle from Human Pluripotent Stem Cells [Internet]. Muscle Cell and Tissue - Current Status of Research Field. IntechOpen; 2018 [cited 2023 Jan 12]. Available from: https://www.intechopen.com/state.item.id

14. Pourquié O, Al Tanoury Z, Chal J. Chapter Five - The Long Road to Making Muscle In Vitro. In: Brivanlou AH, editor. Current Topics in Developmental Biology [Internet]. Academic Press; 2018 [cited 2023 Jan 14]. p. 123–42. (Human Embryonic Stem Cells in Development; vol. 129). Available from: https://www.sciencedirect.com/science/article/pii/S0070215318300462

15. Yan L, Rodríguez-delaRosa A, Pourquié O. Human muscle production in vitro from pluripotent stem cells: Basic and clinical applications. Seminars in Cell & Developmental Biology. 2021 Nov;119:39–48.

16. Chal J, Oginuma M, Al Tanoury Z, Gobert B, Sumara O, Hick A, et al. Differentiation of pluripotent stem cells to muscle fiber to model Duchenne muscular dystrophy. Nat Biotechnol. 2015 Sep;33(9):962–9.

17. Xi H, Fujiwara W, Gonzalez K, Jan M, Liebscher S, Van Handel B, et al. In Vivo Human Somitogenesis Guides Somite Development from hPSCs. Cell Reports. 2017 Feb 7;18(6):1573–85.

18. Hicks MR, Hiserodt J, Paras K, Fujiwara W, Eskin A, Jan M, et al. ERBB3 and NGFR mark a distinct skeletal muscle progenitor cell in human development and hPSCs. Nat Cell Biol. 2018 Jan;20(1):46–57.

19. van der Wal E, Bergsma AJ, van Gestel TJM, in 't Groen SLM, Zaehres H, Araúzo-Bravo MJ, et al. GAA Deficiency in Pompe Disease Is Alleviated by Exon Inclusion in iPSC-Derived Skeletal Muscle Cells. Mol Ther Nucleic Acids. 2017 Mar 14;7:101–15.

20. Borchin B, Chen J, Barberi T. Derivation and FACS-Mediated Purification of PAX3+/PAX7+ Skeletal Muscle Precursors from Human Pluripotent Stem Cells. Stem Cell Reports. 2013 Dec 17;1(6):620–31.

21. Shelton M, Metz J, Liu J, Carpenedo RL, Demers SP, Stanford WL, et al. Derivation and Expansion of PAX7-Positive Muscle Progenitors from Human and Mouse Embryonic Stem Cells. Stem Cell Reports. 2014 Sep 9;3(3):516–29.

22. Caron L, Kher D, Lee KL, McKernan R, Dumevska B, Hidalgo A, et al. A Human Pluripotent Stem Cell Model of Facioscapulohumeral Muscular Dystrophy-Affected Skeletal Muscles. Stem Cells Transl Med. 2016 Sep;5(9):1145–61.

23. Choi IY, Lim H, Estrellas K, Mula J, Cohen TV, Zhang Y, et al. Concordant but Varied Phenotypes among Duchenne Muscular Dystrophy Patient-Specific Myoblasts Derived using a Human iPSC-Based Model. Cell Reports. 2016 Jun 7;15(10):2301–12.

24. Yaffe D, Saxel O. Serial passaging and differentiation of myogenic cells isolated from dystrophic mouse muscle. Nature. 1977 Dec;270(5639):725–7.

25. Blau HM, Chiu CP, Webster C. Cytoplasmic activation of human nuclear genes in stable heterocaryons. Cell. 1983 Apr 1;32(4):1171–80.

26. Sun Y, Duffy R, Lee A, Feinberg AW. Optimizing the structure and contractility of engineered skeletal muscle thin films. Acta Biomaterialia. 2013 Aug 1;9(8):7885–94.

27. Wong CY, Al-Salami H, Dass CR. C2C12 cell model: its role in understanding of insulin resistance at the molecular level and pharmaceutical development at the preclinical stage. Journal of Pharmacy and Pharmacology. 2020 Dec 1;72(12):1667–93.

28. Diokmetzidou A, Tsikitis M, Nikouli S, Kloukina I, Tsoupri E, Papathanasiou S, et al. Chapter Fifteen - Strategies to Study Desmin in Cardiac Muscle and Culture Systems. In: Omary MB, Liem RKH, editors. Methods in Enzymology [Internet]. Academic Press; 2016 [cited 2023 Jan 14]. p. 427–59. (Intermediate Filament Proteins; vol. 568). Available from: https://www.sciencedirect.com/science/article/pii/S0076687915005443

29. Montano M. 2 - Model systems. In: Montano M, editor. Translational Biology in Medicine [Internet]. Woodhead Publishing; 2014 [cited 2023 Jan 14]. p. 9–33. (Woodhead Publishing Series in Biomedicine). Available from: https://www.sciencedirect.com/science/article/pii/B9781907568428500022

30. Andrés V, Walsh K. Myogenin expression, cell cycle withdrawal, and phenotypic differentiation are temporally separable events that precede cell fusion upon myogenesis. Journal of Cell Biology. 1996 Feb 15;132(4):657–66.

31. Milasincic DJ, Dhawan J, Farmer SR. Anchorage-dependent control of muscle-specific gene expression in C2C12 mouse myoblasts. In Vitro CellDevBiol-Animal. 1996 Feb 1;32(2):90–9.

32. Romanazzo S, Forte G, Ebara M, Uto K, Pagliari S, Aoyagi T, et al. Substrate stiffness affects skeletal myoblast differentiation in vitro. Sci Technol Adv Mater. 2012 Nov 23;13(6):064211.

33. Bajaj P, Reddy B, Millet L, Wei C, Zorlutuna P, Bao G, et al. Patterning the differentiation of C2C12 skeletal myoblasts. Integr Biol (Camb). 2011 Sep;3(9):897–909.

34. Takaza M, Moerman KM, Gindre J, Lyons G, Simms CK. The anisotropic mechanical behaviour of passive skeletal muscle tissue subjected to large tensile strain. Journal of the Mechanical Behavior of Biomedical Materials. 2013 Jan 1;17:209–20.

35. Van Loocke M, Lyons CG, Simms CK. Viscoelastic properties of passive skeletal muscle in compression: Stress-relaxation behaviour and constitutive modelling. Journal of Biomechanics. 2008 Jan 1;41(7):1555–66.

36. Jana S, Levengood SKL, Zhang M. Anisotropic Materials for Skeletal-Muscle-Tissue Engineering. Adv Mater. 2016 Dec;28(48):10588–612.

37. Aviss KJ, Gough JE, Downes S. Aligned electrospun polymer fibres for skeletal muscle regeneration. Eur Cell Mater. 2010 May 13;19:193–204.

38. Pichavant C, Pavlath GK. Incidence and severity of myofiber branching with regeneration and aging. Skeletal Muscle. 2014 May 15;4(1):9.

39. Takahashi H, Shimizu T, Nakayama M, Yamato M, Okano T. The use of anisotropic cell sheets to control orientation during the self-organization of 3D muscle tissue. Biomaterials. 2013 Oct 1;34(30):7372–80.

40. Carnes ME, Pins GD. Etching anisotropic surface topography onto fibrin microthread scaffolds for guiding myoblast alignment. Journal of Biomedical Materials Research Part B: Applied Biomaterials. 2020;108(5):2308–19.

41. Flemming RG, Murphy CJ, Abrams GA, Goodman SL, Nealey PF. Effects of synthetic micro- and nano-structured surfaces on cell behavior. Biomaterials. 1999 Mar 1;20(6):573–88.

42. Dugan JM, Gough JE, Eichhorn SJ. Directing the Morphology and Differentiation of Skeletal Muscle Cells Using Oriented Cellulose Nanowhiskers. Biomacromolecules. 2010 Sep 13;11(9):2498–504.

43. Duffy RM, Sun Y, Feinberg AW. Understanding the Role of ECM Protein Composition and Geometric Micropatterning for Engineering Human Skeletal Muscle. Ann Biomed Eng. 2016 Jun 1;44(6):2076–89.

44. Shimizu K, Fujita H, Nagamori E. Micropatterning of single myotubes on a thermoresponsive culture surface using elastic stencil membranes for single-cell analysis. Journal of Bioscience and Bioengineering. 2010 Feb 1;109(2):174–8.

45. Lam MT, Sim S, Zhu X, Takayama S. The effect of continuous wavy micropatterns on silicone substrates on the alignment of skeletal muscle myoblasts and myotubes. Biomaterials. 2006 Aug 1;27(24):4340–7.

46. Huang NF, Lee RJ, Li S. Engineering of aligned skeletal muscle by micropatterning. Am J Transl Res. 2010 Jan 1;2(1):43–55.

47. Guex AG, Kocher FM, Fortunato G, Körner E, Hegemann D, Carrel TP, et al. Fine-tuning of substrate architecture and surface chemistry promotes muscle tissue development. Acta Biomaterialia. 2012 Apr 1;8(4):1481–9.

48. Beldjilali-Labro M, Jellali R, Brown AD, Garcia Garcia A, Lerebours A, Guenin E, et al. Multiscale-Engineered Muscle Constructs: PEG Hydrogel Micro-Patterning on an Electrospun PCL Mat Functionalized with Gold Nanoparticles. International Journal of Molecular Sciences. 2022 Jan;23(1):260.

49. Cakal SD, Radeke C, Alcala JF, Ellman DG, Butdayev S, Andersen DC, et al. A simple and scalable 3D printing methodology for generating aligned and extended human and murine skeletal muscle tissues. Biomed Mater. 2022 Jul 1;17(4):045013.

50. Kim W, Kim G. 3D bioprinting of functional cell-laden bioinks and its application for cell-alignment and maturation. Applied Materials Today. 2020 Jun 1;19:100588.

51. Kim W, Jang CH, Kim GH. A Myoblast-Laden Collagen Bioink with Fully Aligned Au Nanowires for Muscle-Tissue Regeneration. Nano Lett. 2019 Dec 11;19(12):8612–20.

52. Armstrong JPK, Puetzer JL, Serio A, Guex AG, Kapnisi M, Breant A, et al. Engineering Anisotropic Muscle Tissue using Acoustic Cell Patterning. Advanced Materials. 2018;30(43):1802649.

53. Velasco-Mallorquí F, Fernández-Costa JM, Neves L, Ramón-Azcón J. New volumetric CNT-doped gelatin–cellulose scaffolds for skeletal muscle tissue engineering. Nanoscale Adv. 2020 Jul 14;2(7):2885–96.

54. Christensen RK, von Halling Laier C, Kiziltay A, Wilson S, Larsen NB. 3D Printed Hydrogel Multiassay Platforms for Robust Generation of Engineered Contractile Tissues. Biomacromolecules. 2020 Feb 10;21(2):356–65.

55. Kane RS, Takayama S, Ostuni E, Ingber DE, Whitesides GM. Patterning proteins and cells using soft lithography. Biomaterials. 1999 Dec 1;20(23):2363–76.

56. Liu WW, Chen ZL, Jiang XY. Methods for Cell Micropatterning on Two-Dimensional Surfaces and Their Applications in Biology. Chinese Journal of Analytical Chemistry. 2009 Jul 1;37(7):943–9.

57. Théry M. Micropatterning as a tool to decipher cell morphogenesis and functions. Journal of Cell Science. 2010 Dec 15;123(24):4201–13.

58. Hong HJ, Koom WS, Koh WG. Cell Microarray Technologies for High-Throughput Cell-Based Biosensors. Sensors. 2017 Jun;17(6):1293.

59. Strale PO, Azioune A, Bugnicourt G, Lecomte Y, Chahid M, Studer V. Multiprotein Printing by Light-Induced Molecular Adsorption. Advanced Materials. 2016;28(10):2024–9.

60. High-throughput micropatterning on 96 well plates using PRIMO contactless photopatterning system [Internet]. alvéole. [cited 2023 Feb 16]. Available from: https://www.alveolelab.com/?application_note=high-throughput-micropatterning-on-96-well-plates-using-primo-contactless-photopatterning-system

61. Xu F, Beyazoglu T, Hefner E, Gurkan UA, Demirci U. Automated and Adaptable Quantification of Cellular Alignment from Microscopic Images for Tissue Engineering Applications. Tissue Engineering Part C: Methods. 2011 Jun;17(6):641–9.

62. Kemeny SF, Clyne AM. A Simplified Implementation of Edge Detection in MATLAB is Faster and More Sensitive than Fast Fourier Transform for Actin Fiber Alignment Quantification. Microscopy and Microanalysis. 2011 Apr;17(2):156–66.

63. Ayres CE, Jha BS, Meredith H, Bowman JR, Bowlin GL, Henderson SC, et al. Measuring fiber alignment in electrospun scaffolds: a user's guide to the 2D fast Fourier transform approach. Journal of Biomaterials Science, Polymer Edition. 2008 Jan 1;19(5):603–21.

64. Sharma M. Extracting cell and fibre orientation from microscopic images: computational methods and tools. Current Science. 2016;111(12):1936–45.

65. Cao X, Mircea M, Hil FE van den, Mei H, Neumann K, Anastassiadis K, et al. Tissue microenvironment dictates the state of human induced pluripotent stem cell-derived endothelial cells of distinct developmental origin in 3D cardiac microtissues [Internet]. bioRxiv; 2022 [cited 2023 Jan 23]. p. 2022.11.22.517426. Available from: https://www.biorxiv.org/content/10.1101/2022.11.22.517426v2

66. Marcotti S, Belo de Freitas D, Troughton LD, Kenny FN, Shaw TJ, Stramer BM, et al. A Workflow for Rapid Unbiased Quantification of Fibrillar Feature Alignment in Biological Images. Frontiers in Computer

Science [Internet]. 2021 [cited 2023 Jan 25];3. Available from: https://www.frontiersin.org/articles/10.3389/fcomp.2021.745831

67. Rezakhaniha R, Agianniotis A, Schrauwen JTC, Griffa A, Sage D, Bouten CVC, et al. Experimental investigation of collagen waviness and orientation in the arterial adventitia using confocal laser scanning microscopy. Biomech Model Mechanobiol. 2012 Mar;11(3–4):461–73.

68. Manus MC. Alvéole PRIMO protocol: High-throughput micropatterning on 96 well plates [Internet]. alvéole. 2019 [cited 2023 Jan 23]. Available from: https://www.alveolelab.com/high-throughput-micropatterning-96-well-plates/

69. Chal J, Al Tanoury Z, Hestin M, Gobert B, Aivio S, Hick A, et al. Generation of human muscle fibers and satellite-like cells from human pluripotent stem cells in vitro. Nat Protoc. 2016 Oct;11(10):1833–50.

70. Matsuda M, Yamanaka Y, Uemura M, Osawa M, Saito MK, Nagahashi A, et al. Recapitulating the human segmentation clock with pluripotent stem cells. Nature. 2020 Apr;580(7801):124–9.

71. Stepwise in vitro induction of human somitic mesoderm and its derivatives [Internet]. 2020 [cited 2023 Feb 12]. Available from: https://www.researchsquare.com

72. Wan LQ, Chin AS, Worley KE, Ray P. Cell chirality: emergence of asymmetry from cell culture. Philos Trans R Soc Lond B Biol Sci. 2016 Dec 19;371(1710):20150413.

73. Wan LQ, Ronaldson K, Park M, Taylor G, Zhang Y, Gimble JM, et al. Micropatterned mammalian cells exhibit phenotype-specific left-right asymmetry. Proceedings of the National Academy of Sciences. 2011 Jul 26;108(30):12295–300.